

Directional Manipulation of a Staggered Charge Density Wave and Kondo Resonance in UTe_2

Nileema Sharma^{1,2†}, Fangjun Cheng^{1,2†}, Hyeok Jun Yang^{1†}, Matthew Toole^{1,2}, James McKenzie^{1,2}, Mitchell M. Bordelon³, Sean M. Thomas³, Priscila F. S. Rosa³, Yi-Ting Hsu^{1*}, and Xiaolong Liu^{1,2*}

¹*Department of Physics and Astronomy, University of Notre Dame, Notre Dame, IN 46556, USA*

²*Stavropoulos Center for Complex Quantum Matter, University of Notre Dame, Notre Dame, IN 46556, USA*

³*Los Alamos National Laboratory, Los Alamos, New Mexico 87545, USA*

* Corresponding authors. yhsu2@nd.edu, xliu33@nd.edu

† These authors contributed equally to this work.

Abstract

UTe_2 is a rare example of a correlated quantum material in which unconventional density wave orders, Kondo physics, spin-triplet pairing, and reentrant superconductivity coexist within the same electronic system. Its superconducting state develops out of a strongly correlated normal phase. The identification and control of competing or intertwined normal-state orders are thus central to elucidating the electronic landscape from which its superconductivity arises. Here, using scanning tunnelling microscopy (STM) in a vector magnetic field, we uncover a previously unreported staggered charge-density-wave (CDW) in high-quality UTe_2 crystals and demonstrate its strong directional response to an external magnetic field: the staggered CDW is completely quenched by a modest 1.7 T field aligned with the quasi-one-dimensional uranium chain direction (a -axis), while remaining robust against fields along other crystallographic directions. This pronounced anisotropy is consistent with an orbital-driven mechanism that leads to a field-tuned quantum phase transition. Strikingly and counterintuitively, the same field orientation and strength concomitantly alter the hybridization gap and suppress the $5f$ Kondo resonance. Modelling indicates that this correlated evolution arises from a switch of the dominant hybridization channel from Te $5p$ - U $5f$ to U $6d$ - U $5f$ coupling, suggesting an intimate interplay between CDW and the Kondo effect. Our work establishes an effective tuning knob for the intertwined orders in UTe_2 and provides evidence for orbital-selective Kondo hybridization, shedding light on its correlated normal state.

Main

Strongly correlated materials often exhibit a complex landscape of intertwined orders in which multiple broken-symmetry phases can emerge and compete under external tuning parameters, such as temperature, doping, pressure, and magnetic field^{1,2}. This paradigm is epitomized by the high-temperature cuprate superconductors, where charge/spin orders, nematicity, pseudogap behavior, and superconductivity are intricately entangled across their phase diagrams^{3,4}, yet the interplay between density waves and *d*-wave superconductivity remains an open question⁵. Recently, the heavy-fermion superconductor UTe₂ has emerged as a leading candidate for bulk spin-triplet superconductivity⁶, possessing exceptionally large upper critical fields⁷, re-entrant and field-reinforced superconducting phases⁸, exotic vortex structures^{9,10,11}, and the existence of antiferromagnetic spin correlations¹². As in the cuprates, its normal state is highly nontrivial and likely bears an intimate connection to the properties of the superconducting state. Notably, UTe₂ simultaneously hosts charge density wave (CDW) order^{13,14,15,16} and Kondo lattice physics¹⁷—an unusual coexistence, as both phenomena typically compete for spectral weight near the Fermi level¹⁸. Previous work has shown that the CDW in UTe₂ exhibits unconventional behavior, including being sensitive to high magnetic fields of ~10 T applied nearly along the [011] direction^{13,15,16}. At the same time, theoretical studies suggest that Kondo hybridization in UTe₂ is orbital selective, involving U-5*f* states coupled to either Te-5*p* or U-6*d* orbitals¹⁹; however, experimental evidence supporting this scenario has not yet been established. These observations raise several key questions: How do CDW order and Kondo hybridization interact within the highly anisotropic electronic structure of UTe₂? How are these interactions modified by external perturbations such as magnetic fields? And can magnetic-field tuning reveal signatures of orbital-selective Kondo hybridization?

Structurally, UTe₂ is composed of quasi-one-dimensional (1D) atomic chains extending along the crystallographic *a*-axis (Fig. 1a, inset). This low-dimensional architecture gives rise to two orthogonally oriented sets of hybridized quasi-1D Fermi surfaces derived predominantly from Te-5*p* and U-6*d* orbitals (Supplementary Fig. 1)²⁰. In such quasi-1D systems, both the Pauli and orbital effects play essential roles in governing the directional response of charge order to external magnetic fields^{21,22,23,24,25,26}. The Pauli effect, arising from spin splitting, is largely isotropic and tends to suppress CDW orders^{21,22}. By contrast, the orbital effect on CDW depends sensitively on the orientation of the magnetic field relative to the 1D chains, owing to the anisotropic electronic dispersion^{21,22}. Given the generally competing nature of CDW order and Kondo screening^{18,27}, together with the pronounced structural anisotropy and orbital-selective Kondo hybridization in UTe₂, the influence of a vector magnetic field on these intertwined phenomena is expected to be highly nontrivial, yet completely unexplored.

Here, using spectroscopic-imaging scanning tunneling microscopy (SI-STM) on high-quality UTe₂ single crystals with a critical temperature $T_c = 2.1$ K, we discover a new CDW order forming a staggered, brick-wall-like modulation in real space. By applying a 3D vector magnetic

field, we uncover an exceptionally strong directional field response of both the staggered CDW and Kondo resonance. While the CDW and Kondo spectral features remain virtually unaltered under magnetic fields up to 8.8 T applied perpendicular to the (011) surface, the staggered CDW undergoes a field-driven quantum phase transition and becomes completely suppressed when a comparatively modest field of 1.7 T is rotated toward the crystallographic a -axis in the normal state. Notably, and counter to conventional expectations, the Kondo resonance is simultaneously suppressed as the CDW vanishes. The concomitant suppression of the staggered CDW and the Kondo resonance with a -axis magnetic field is consistent with field-induced orbital effects and the existence of orbital-selective Kondo effects in UTe₂. More specifically, an a -axis field destabilizes the staggered CDW, which is derived from nesting with quasi-1D U- $6d$ bands, and shifts the dominant Kondo hybridization from p - f to d - f channels.

Discovery of a new staggered CDW

Cryogenic cleaving of UTe₂ single crystals exposes the (011) plane as shown in Fig. 1a. Differential conductance imaging [$g(\mathbf{r}, V) \equiv dI/dV$], proportional to the local density of states (LDOS), resolves not only the Te atomic lattice (Fig. 1b), but additional modulation wavevectors as most clearly seen in the Fourier transform image $g(\mathbf{q}, 10 \text{ mV})$ in Fig. 1c acquired at 0.3 K. In addition to the previously reported^{13,14,15,16} CDW wavevectors Q_i , we discovered a new set of distinct wavevectors W_i , where $i = 1, 2, 3$. These wavevectors are non-dispersive with energy and exhibit contrast inversion across zero bias (Supplementary Fig. 2) – behavior characteristic of CDWs arising from Fermi surface nesting and accompanied by a gap opening at the Fermi level^{28,29}. These observations establish W_i as a new set of CDWs in UTe₂ with $W_{1,3} = (\mp \frac{2\pi}{b^*}, 0.13 \frac{2\pi}{a})$, where a and b^* are defined in Fig. 1a inset. By visualizing the thermal melting of both W_i and Q_i CDWs, we determined that the W_i CDWs persist into the normal state of UTe₂ with a critical temperature $T_{\text{CDW}}^{W_i} \sim 6 \text{ K}$ (Supplementary Figs. 3). At the bias where the W_i CDW intensity peaks (3.33 mV, Fig. 1d), the real-space pattern forms a staggered, brick-wall-like modulation, with periodic hotspots arranged alternately along neighboring Te chains (Fig. 1e). This structure closely resembles Coulomb coupled 1D CDWs³⁰ described by the Šaub-Barišić-Friedel model³¹, suggesting the quasi-1D nature of the W_i CDW. Consistent with this picture, both W_i and Q_i wavevectors connect segments of the warped quasi-1D U-derived bands³² and lie on the edges of the surface Brillouin zone (Supplementary Fig. 1), analogous to quasi-1D CDWs in organic conductors³³ from Fermi surface nesting. Furthermore, spatial correlations between the mirror symmetric W_1 (Q_1) and W_3 (Q_3) modulations are observed (Supplementary Figs. 4,5). Compared to W_1 and W_3 , the W_2 wavevector has a much lower intensity close to background noise (Fig. 1c,f), possibly due to the presence of quenched disorders and/or the formfactor of W_i CDW (Supplementary Fig. 6). Thus, we focus on W_1 and W_3 in this study. Although $Q_1 \cong W_1 + W_2$, the set of W_i CDW constitutes an independent electronic order because W_i and Q_i CDWs exhibit vastly different energy dependence of their intensities (Fig. 1d), critical temperatures, critical fields (Fig. 3), as well as uncorrelated spatial distributions of topological defects (Supplementary Figs. 4, 5).

Insensitivity of CDW and Kondo resonance to out-of-plane magnetic fields

Having established the new W_i CDW order, we explore the effect of an out-of-plane magnetic field B_{\perp} along the (011) surface normal direction (defined as c^* -axis, Fig. 1a inset). Figure 1d compares the energy-dependence of the W_1 and Q_1 intensities under different B_{\perp} and field-sweep directions. The nearly overlapping curves suggest their minimal sensitivity to an out-of-plane magnetic field up to 8.8 T. This robustness is better illustrated in Fig. 2a, where the integrated intensities of W_1 (at $V = 3.33$ mV) and Q_1 (at $V = 10$ mV) in momentum space, corresponding to their respective peak amplitudes, remain essentially unchanged across the entire field range. Real-space $g(\mathbf{r}, V)$ and the extracted CDW amplitude/phase images of the same field of views (FOVs) under different B_{\perp} likewise show no obvious evolution with B_{\perp} (Supplementary Figs. 4,5), further demonstrating the robustness and reproducibility of our STM imaging. The insensitivity of the CDWs to B_{\perp} is consistent with the negligible theoretical reduction $\Delta T_{\text{CDW}} = -\frac{\gamma}{4} \left(\frac{\mu_B B}{kT_{\text{CDW}}(0)} \right)^2 T_{\text{CDW}}(0)$ due to the Pauli effect^{21,22}. Here, γ is of order 1. For $T_{\text{CDW}}^{W_i} \approx 6$ K and $T_{\text{CDW}}^{Q_i} \approx 10$ K (Supplementary Fig. 3), the Pauli-limiting fields are approximately $B_P^{W_i} \approx 18$ T and $B_P^{Q_i} \approx 30$ T, respectively. Indeed, the Q_i CDW has recently been detected³⁴ even at $B_{\perp} = 20$ T.

We next examine the influence of B_{\perp} on the Kondo effect in UTe_2 spectroscopically. Figure 2b presents a set of spatially averaged differential conductance spectra measured at 0.3 K under different B_{\perp} , exhibiting virtually identical spectra with a broad spectral bump near -4 mV (red arrow) and a dip at zero bias. The bump is consistent with previously reported¹⁷ Kondo resonance signature in UTe_2 . After subtracting a linear background (see Methods), this spectral feature resolves into two peaks that are ~ 2 mV apart as indicated by the blue and green arrows in Fig. 2c. These two peaks are characteristic of a Kondo lattice^{35,36}, arising from hybridization between a light conduction band (grey) and a heavy f -electron band (blue) (inset of Fig. 2c), which produces asymmetric coherence peaks separated by a hybridization gap Δ_h . The extracted peak heights ($H_{1,2}$) and hybridization gap exhibit negligible variation with B_{\perp} up to 8.8 T (Fig. 2d), indicating that Kondo coherence remains robust, consistent with behaviors observed in other heavy-fermion systems under comparable field strengths^{37,38}.

We further examine whether the staggered CDW is coupled to or competes with spin-triplet superconductivity in UTe_2 . To this end, we image vortex lattices (VLs) generated under identical magnetic fields but separate field cooling procedures. Because individual vortices – where superconductivity is locally suppressed – nucleate at different spatial locations in repeated field-cooling cycles, this approach enables us to test whether the CDW responds to local suppression of superconductivity. As shown in Figs. 2e,f, vortices in UTe_2 exhibit a characteristic doublet structure^{9,10,11}, and the two triangular VLs created at $B_{\perp} = 8.8$ T are clearly displaced from each other in the zero-bias conductance images [$g(\mathbf{r}, 0\text{ V})$ and $g'(\mathbf{r}, 0\text{ V})$] of the same field of view. The images are registered to each other via a multi-image registration procedure (see Methods).

However, the corresponding $g(\mathbf{r}, 3.33 \text{ mV})$ images, where the staggered W_i CDW is most pronounced, show virtually no changes (Figs. 2g,h). This is further confirmed by examining the difference maps [$\delta g(\mathbf{r}, V) \equiv g(\mathbf{r}, V) - g'(\mathbf{r}, V)$] in Figs. 2i,j: while $\delta g(\mathbf{r}, 0 \text{ V})$ clearly reflects the displaced VL lattice, the $\delta g(\mathbf{r}, 3.33 \text{ mV})$ image is essentially noise. Moreover, phase-resolved analysis using a 2D lock-in algorithm (see Methods) shows that the spatial phase $\Phi_{W_1}(\mathbf{r})$ of the W_1 CDW and its associated topological defects in the form vortices and anti-vortices³⁹ (indicated by the white and black dots, respectively) remain unchanged (Figs. 2k,l). This further confirms that the W_i CDW is insensitive to local suppression of superconductivity and thus couples only weakly to uniform superconductivity.

Simultaneous manipulation of CDW and Kondo resonance with an in-plane magnetic field

Next, we investigate the responses of CDW and Kondo effect to a vector magnetic field \mathbf{B}_{\parallel} applied in the (011) plane with an angle θ from the a -axis. Figure 3a displays a series of $g(\mathbf{q}, 3.33 \text{ mV})$ images that capture the evolution of W_i CDW as \mathbf{B}_{\parallel} is rotated within the plane at 2.5 K [full sets of $g(\mathbf{r}, 3.33 \text{ mV})$, $g(\mathbf{r}, 10 \text{ mV})$ and their Fourier transforms for θ varying between 0 and 2π are given in Supplementary Figs. 7,8]. Remarkably, although the field strength $B_{\parallel} = 1.7 \text{ T}$ is moderate, a complete (strong) suppression of the staggered W_i (Q_i) CDW is observed when \mathbf{B}_{\parallel} is parallel to the a -axis ($\theta = 0$) of UTe_2 , whereas virtually no effects are present when \mathbf{B}_{\parallel} is perpendicular ($\theta = \pi/2$) to the a -axis (defined as the b^* -axis, Fig. 1a inset; Supplementary Fig. 9). Such highly directional response of CDW to \mathbf{B}_{\parallel} is reproduced at 0.3 K (Supplementary Fig. 10). Spectroscopically, this suppression of CDW manifests as a pronounced angular modulation of the low-bias conductance (Fig. 3b). At $\theta = 0$ and π , where the field is parallel to the uranium chains and the CDW is maximally suppressed, the zero-bias conductance increases substantially. Since UTe_2 is in the normal state at 2.5 K, such changes are unrelated to superconductivity, but consistent with the closing of CDW gaps around the Fermi level⁴⁰. Real-space maps (Fig. 3c) show that the brick-wall modulation amplitude from W_i CDW continuously diminishes as the field rotates toward the a -axis, yielding a two-fold symmetric suppression of CDW intensity (Figs. 3f,g). CDW amplitude $A_{W_1}(\mathbf{r})$ and phase $\Phi_{W_1}(\mathbf{r})$ analysis (Figs. 3d,e) reveals that domains of high CDW amplitude shrink in size without a proliferation of topological defects, indicating that the quantum melting of the CDW is driven by a reduction of the electron–hole pairing amplitude rather than by a loss of phase stiffness^{41,42}. This behavior is consistent with the suppression of $T_{\text{CDW}}^{W_i}$ to zero at a critical in-plane field B_c along the a -axis of UTe_2 .

Anisotropy of the Pauli effect cannot fully account for such observations. Although the magnetic susceptibility χ of UTe_2 along the magnetic easy axis (a -axis) is about 5 times larger than those along perpendicular directions at temperatures approaching zero⁴³, the corresponding Pauli paramagnetic limit $B_P = 2\Delta_0/\sqrt{2}g\mu_B \propto 1/\sqrt{\chi}$ (where Δ_0 is the CDW gap, g is the g -factor of electrons) is reduced only by a factor of 0.45 along the a -axis⁴⁴, insufficient to explain why $B_{\parallel} = 1.7 \text{ T}$ along the a -axis fully quenches the CDW, whereas $B_{\perp} = 8.8 \text{ T}$ along the c^* -axis

produces no discernable effects. Another possible mechanism is a magnetic field induced Lifshitz transition. While such Fermi surface reconstructions have been observed⁴⁵ at the metamagnetic transitions of UTe₂ at ~ 35 T, low-field transport anomalies⁴⁶ appear only above fields of 5.6 T along the a -axis, making Lifshitz transition unlikely to account for the observed CDW suppression with $B_{\parallel} = 1.7$ T. By contrast, it has been established both theoretically^{21,23,24} and experimentally^{22,25,26} that when an external magnetic field is applied perpendicular or parallel to the chains of a quasi-1D system, the CDW therein will be stabilized or suppressed, respectively, resulting from confined orbital motion of charges. In UTe₂, the 1D uranium chains run along the a -axis while both the b^* - and c^* - axes are transverse to the chains. It is therefore plausible to suspect that the orbital effect of electrons is responsible for the observed highly anisotropic response of CDW to vector magnetic fields. To better visualize this behavior, we map the integrated intensities of W_i and Q_i CDWs in the phase space of B_{\parallel} , θ , and T , as shown in Figs. 3h,i. The phase boundaries defining the CDW states are determined by fitting the experimental integrated intensity of CDW peaks (details given in Methods), and the CDW occupy the phase space with $T \rightarrow 0$, $B_{\parallel} \rightarrow 0$, and $\theta \rightarrow \pi/2$ as shown in Figs. 3h,i. For W_1 CDW, the fitting yields a zero-temperature critical field of $B_c^{W_1}(T=0) \approx 1.7$ T along the a -axis, consistent with experimental observations (Fig. 2) and the fact that W_i is not fully suppressed at $B_{\parallel} = 1.5$ T along the a -axis at 0.3 K (Supplementary Fig. 10). These results point to a putative quantum critical point, beyond which the W_i CDW becomes quantum disordered at zero temperature.

In light of the potential interplay between CDW orders and Kondo physics, it is worthwhile to examine how \mathbf{B}_{\parallel} simultaneously influences the Kondo resonance. Figure 4a presents a series of spatially averaged dI/dV spectra acquired at 0.3 K (for optimal energy resolution) on a different UTe₂ crystal under an in-plane magnetic field of $B_{\parallel} = 1.95$ T, while the angle θ between \mathbf{B}_{\parallel} and the a -axis is varied from 0 to 2π . Consistent with the behavior observed at 2.5 K (Fig. 3b), the zero-bias conductance increases when the CDW is suppressed at $\theta = 0$ and π , and decreases when it is restored at $\theta = \pi/2$ and $3\pi/2$ as indicated by the orange curve. Meanwhile, the Kondo resonance feature around -4 mV exhibits an opposite angular modulation as indicated by the blue curve. After subtracting a linear background (Fig. 4b), the modulation of the Kondo resonance becomes more evident in the extracted peak heights ($H_{1,2}$) and the hybridization gap (Δ_h). The polar plots in Figs. 4c,d demonstrate an in-phase modulation between H_1 and H_2 , and an out-of-phase modulation between $H_{1,2}$ and Δ_h as θ is varied from 0 to 2π . Notably, the relative amplitudes of H_1 and H_2 invert between $\theta = 0$ (or π) and $\theta = \pi/2$ (or $3\pi/2$).

Analogous to the response of CDW to \mathbf{B}_{\parallel} , the anisotropic Pauli effect alone is unlikely to account for this pronounced directional modulation by \mathbf{B}_{\parallel} , particularly given the insensitivity of the Kondo resonance to B_{\perp} up to 8.8 T. The distinct angular evolution of $H_{1,2}$ and Δ_h further points to an additional mechanism. Because both Te-5*p* and U-6*d* itinerant electrons can participate in Kondo screening¹⁹ that competes with CDW formation^{18,27}, and because both the W_i and Q_i

CDWs likely originate from nesting of the U-6*d* bands (Supplementary Fig. 1), the formation of CDW weakens the overall Kondo screening by U-6*d*-electrons. In contrast, the itinerant *p*-electrons provide a uniform charge background irrespective of the presence of CDWs. It is therefore reasonable to infer that, when CDWs are present, the dominant Kondo hybridization occurs in the *p*-*f* channel. When the CDWs are suppressed, the proximity between U-6*d* and U-5*f* orbitals renders an effective shift in the dominant hybridization channel to *d*-*f*, as illustrated schematically in Figs. 4e,f. With physically reasonable parameters specific to UTe₂, we construct a minimal theoretical model incorporating this hybridization reconfiguration proposal (see details in Methods). The model qualitatively reproduces the key experimental signatures in calculated *dI/dV* spectra (Fig. 4g), including the modulation of $H_{1,2}$ and Δ_h , as well as the inversion in the relative peak heights of H_1 and H_2 between the CDW and CDW-suppressed states. Although field-induced modifications of exchange coupling likely also contribute⁴⁷, they are not a necessary ingredient in our model to reproduce the experimental observations, and a more detailed material-specific microscopic treatment for UTe₂ is required to elucidate its role. Therefore, the simultaneous tuning of CDW and Kondo resonance provides direct evidence supporting the orbital-selectivity of the Kondo effect in UTe₂.

Conclusion

In this work, we discovered a new set of W_i CDW with a staggered real-space structure in high-quality UTe₂ crystals. We demonstrate that both the staggered CDW and Kondo coherence are insensitive to magnetic fields applied perpendicular to the quasi-1D chains, yet are concomitantly suppressed by a modest field aligned along the *a*-axis, revealing a putative CDW quantum critical point at $B_{\parallel} \approx 1.7$ T. Such pronounced vector-field tuning of CDW and Kondo resonance cannot be accounted for by the Pauli effects alone and instead point to an orbital-driven mechanism and a modification of the dominant Kondo hybridization channels. These observations provide direct evidence for orbital-selective Kondo hybridization and intertwined charge order and Kondo screening in UTe₂. Because the W_i CDW persist in the superconducting state of UTe₂, it necessarily induces a set of composite spin-triplet pair density waves (PDWs) with the same wavevectors even if the CDWs do not couple strongly to superconductivity (Fig. 2). Our results therefore imply a concomitant magnetic field tuning of such composite PDWs, which deserves future investigation. Overall, our work demonstrates that directional magnetic fields are a powerful tuning knob for controlling emergent order and probing the couplings between them. Our findings also introduce charge order and hybridization switching as key ingredients of the normal state phase diagram of UTe₂.

Methods

1. Crystal synthesis and STM measurements

As in our previous study⁹, high quality UTe₂ crystals with $T_c = 2.1$ K are grown using a molten salt flux method and are polished along the (011) direction for mechanical cleaving. The UTe₂ crystals are cleaved at cryogenic temperature (~ 10 K) under ultra-high vacuum ($<$

1×10^{-10} Torr) conditions and immediately transferred into the scan head of a Unisoku USM1300J microscope. Mechanically cut Nb wires are used as STM tips after outgassing in ultra-high vacuum conditions. As prepared tips are superconducting under zero magnetic field, but become normal under a magnetic field of 1 T (Supplementary Fig. 11). Therefore, for all data taken under non-zero field in this study, the tip is metallic to eliminate complexities associated with tip superconductivity. All STM measurements are performed using SPECS Nanonis electronics with a built-in lock-in amplifier. MATLAB and Gwyddion software are used for processing the acquired data.

2. Image correction and registration with sub-atomic precision

Because of the ubiquitous thermal drifts and artifacts associated with the piezoelectric scanner in an STM, images taken in nominally identical FOVs but from separate measurements need to be precisely registered with each other with sub-atomic precision to enable rigorous extraction and comparisons of CDW intensity and spatially resolved modulation amplitude, phase, and topological defects. This is achieved in three steps: firstly, the raw experimental images are up-sampled by a factor of four. Secondly, the Lawler-Fujita (LF) algorithm⁴⁸ and shear transformation are applied to restore a periodic atomic lattice from experimental images that contain distortions due to thermal and piezoelectric drifts. Lastly, affine transformations are applied to register multiple images to the same FOV with sub-atomic precision.

A perfectly periodic lattice $\tilde{T}(\tilde{\mathbf{r}})$ with Bragg wavevectors $\mathbf{B}_i = (B_i^x, B_i^y)$, where $i = 1, 2, 3$, can be written as

$$\tilde{T}(\tilde{\mathbf{r}}) = \sum_{i=1}^3 T_i \cos(\mathbf{B}_i \cdot \tilde{\mathbf{r}} + \bar{\varphi}_i)$$

Here, $\bar{\varphi}_i$ represents the constant spatial phase shift along \mathbf{B}_i . Experimentally, the STM topographic image $T(\mathbf{r})$ suffers from a slowly varying \mathbf{r} -dependent spatial phase shift $\varphi_i(\mathbf{r})$, leading to

$$T(\mathbf{r}) = \sum_{i=1}^3 T_i \cos(\mathbf{B}_i \cdot \mathbf{r} + \varphi_i)$$

To extract $\varphi_i(\mathbf{r})$, experimental topographic image $T(\mathbf{r})$ is multiplied by a reference wave $e^{i\mathbf{B}_i \cdot \mathbf{r}}$ and integrated over a Gaussian filter with width $\sigma = 1.64$ nm (i.e., a few lattice constants) to obtain the complex-valued $A_{\mathbf{B}_i}(\mathbf{r})$

$$A_{\mathbf{B}_i}(\mathbf{r}) = \frac{1}{\sqrt{2\pi}\sigma} \int d\mathbf{R} T(\mathbf{R}) e^{i\mathbf{B}_i \cdot \mathbf{R}} e^{-\frac{(\mathbf{r}-\mathbf{R})^2}{2\sigma^2}}$$

Such a convolution integral can be conveniently calculated by using the convolution theorem

$$A_{\mathbf{B}_i}(\mathbf{r}) = F^{-1}[\tilde{A}_{\mathbf{B}_i}(\mathbf{q})] = F^{-1}\left[F(T(\mathbf{r})e^{i\mathbf{B}_i \cdot \mathbf{r}}) \frac{1}{\sqrt{2\pi}\sigma_q} e^{-\frac{\mathbf{q}^2}{2\sigma_q^2}}\right]$$

where F and F^{-1} denote Fourier transform and inverse Fourier transform, respectively, and $\sigma = 1/\sigma_q$. Then we can obtain

$$\varphi_i(\mathbf{r}) = \tan^{-1} \left\{ \frac{\text{Im}[A_{B_i}(\mathbf{r})]}{\text{Re}[A_{B_i}(\mathbf{r})]} \right\}$$

Because the relationship between the distorted and the perfect Bragg lattice for each B_i is

$$B_i \cdot \mathbf{r} + \varphi_i(\mathbf{r}) = B_i \cdot \tilde{\mathbf{r}} + \bar{\varphi}_i$$

, we can define a displacement field $\mathbf{u}(\mathbf{r}) = \mathbf{r} - \tilde{\mathbf{r}}$ and write it in the matrix form

$$B\mathbf{u}(\mathbf{r}) = \bar{\varphi} - \varphi(\mathbf{r})$$

where $B = (B_1 \ B_2 \ B_3)^T$ is a 3×2 matrix that is left-invertible, $\mathbf{u}(\mathbf{r}) = (u_1(\mathbf{r}) \ u_2(\mathbf{r}) \ u_3(\mathbf{r}))^T$ and $\bar{\varphi} - \varphi(\mathbf{r}) = (\bar{\varphi}_1 - \varphi_1(\mathbf{r}) \ \bar{\varphi}_2 - \varphi_2(\mathbf{r}) \ \bar{\varphi}_3 - \varphi_3(\mathbf{r}))^T$ are two column vectors. Therefore, we can obtain

$$\mathbf{u}(\mathbf{r}) = B^{-1}(\bar{\varphi} - \varphi(\mathbf{r}))$$

The choice of $\bar{\varphi}_i$ is arbitrary. A nearly perfectly periodic image can be obtained as $T(\mathbf{r} + \mathbf{u}(\mathbf{r}))$. Such LF-corrected image is then sheared, which can be represented by a transformation matrix $S = \begin{bmatrix} 1 & p \\ 0 & 1 \end{bmatrix}$, to obtain a periodic and symmetric lattice.

Lastly, to register multiple images to the exact same FOV, we first define three reference points in each image (e.g., three atomic defects). Using one LF- and shear-corrected image as the reference, an affine transformation matrix

$$\begin{bmatrix} x' \\ y' \\ 1 \end{bmatrix} = \begin{bmatrix} a & b & e \\ c & d & f \\ 0 & 0 & 1 \end{bmatrix} \begin{bmatrix} x \\ y \\ 1 \end{bmatrix}$$

is determined by requiring the 3 reference points in an image to be registered with the ones in the reference image after the affine transformation. Then, the same affine transformation is applied to the entire image.

3. CDW phase and amplitude extraction

A periodic modulation of the differential conductance due to CDW with wavevector \mathbf{Q} can be expressed as

$$g(\mathbf{r}) = A_{\mathbf{Q}}(\mathbf{r}) \cos(\mathbf{Q} \cdot \mathbf{r} + \Phi_{\mathbf{Q}}(\mathbf{r})) + g_0$$

with amplitude of modulation $A_{\mathbf{Q}}$, spatially dependent phase $\Phi_{\mathbf{Q}}$, and a constant background g_0 . To extract $A_{\mathbf{Q}}$ and $\Phi_{\mathbf{Q}}$, we use a computational 2D-lockin technique similar to that applied in the LF algorithm. Firstly, $g(\mathbf{r})$ is multiplied by a reference signal $e^{i\mathbf{Q} \cdot \mathbf{r}}$ with identical periodicity with the CDW. Then it is integrated over the entire FOV to obtain the complex valued $g_{\mathbf{Q}}(\mathbf{r})$

$$g_{\mathbf{Q}}(\mathbf{r}) = \frac{1}{\sqrt{2\pi\sigma}} \int g(\mathbf{R}) e^{-\frac{|\mathbf{r}-\mathbf{R}|^2}{2\sigma^2}} e^{-i\mathbf{Q} \cdot \mathbf{R}} d\mathbf{R}$$

, which similarly is calculated in the momentum space using the convolution theorem. Here, σ is the radius of a Gaussian filter in real space that has to be larger than $2\pi/Q$ (i.e., larger than the period) but small enough such that the equivalent \mathbf{q} -space filter covers the peak at \mathbf{Q} in the FT to avoid artificial truncation of the signal. Considering the length scale of the CDWs, we used Gaussian widths $\sigma_{Q_i} = 1.80$ nm and $\sigma_{W_i} = 2.45$ nm for the Q_i and W_i CDW, respectively. The phase $\Phi_{\mathbf{Q}}(\mathbf{r})$ is therefore obtained as

$$\Phi_{\mathbf{Q}}(\mathbf{r}) = \tan^{-1} \left\{ \frac{\text{Im}[g_{\mathbf{Q}}(\mathbf{r})]}{\text{Re}[g_{\mathbf{Q}}(\mathbf{r})]} \right\}$$

The CDW modulation amplitude $A_{\mathbf{Q}}(\mathbf{r})$ at location \mathbf{r} is thus given by the amplitude $|g_{\mathbf{Q}}(\mathbf{r})|$. If $\Phi_{\mathbf{Q}}(\mathbf{r})$ is outside $[0, 2\pi]$, it is brought into this range by $\Phi_{\mathbf{Q}}(\mathbf{r}) \rightarrow \text{mod}[\Phi_{\mathbf{Q}}(\mathbf{r}), 2\pi]$.

4. CDW intensity extraction

FTs of registered conductance maps measured in the same FOV are used for analyzing the intensity of the CDW wavevectors (Q_i and W_i). The CDW peak intensity (e.g., Fig. 1d) is determined by locating the maximum intensity of the corresponding wavevector in the FT, and integrate the intensity within a circular region with a 3-pixel (5.58 nm^{-1}) radius, which is large enough to include the entire CDW signal but not covering unrelated momentum space features. In temperature dependent measurements (Supplementary Fig. 3), the W_i CDW intensity was found to be within the noise floor at $T = 7$ K. Given the greater background signal at such low- \mathbf{q} regions, the intensity obtained under this condition was defined as the background level and was subtracted from all W_i CDW intensity measurements. Since the Q_i CDW have much larger q , the background signal is significantly lower and thus we choose not to subtract any background.

5. Plotting the CDW phase boundaries

Since the a -axis magnetic field is the non-thermal parameter controlling the CDWs, the W_i and Q_i CDW intensities can be fitted using the power law^{49,50}

$$I(B_p, T) = I_0 \left(1 - \frac{T}{T_c(B_p)} \right)^{2\beta(B_p)}$$

where $B_p = B \cos \theta$, $T_c(B_p) = T_c(0) \left(\frac{B_c - B_p}{B_c} \right)$ (ref. 49,50,51), and we approximate $\beta(B_p)$ using a third order polynomial $\beta(B_p) = aB_p^3 + bB_p^2 + cB_p + d$. Here, B_c , $T_c(0)$, a , b , c and d are the fitting parameters. The fitted parameters for Q_1 are $B_c = 2.67 T$, $T_c(0) = 10.18$ K, $\beta(B_p) = -0.707B_p^3 + 2.08B_p^2 - 1.51B_p + 0.465$, and $I_0 = 10.8$. The fitted parameters for W_1 are $B_c = 1.73 T$, $T_c(0) = 6.03$ K, $\beta(B_p) = 0.0792B_p^3 + 0.266B_p^2 - 0.5B_p + 0.193$, and $I_0 = 3.54$. The phase boundaries shown in Figs. 3h,i are defined by letting $I(B_p, T) = 0$.

6. Extracting experimental Kondo resonance peak features

To quantify the energy positions and heights of the two Kondo-related spectral features, we first smoothen the experimental differential conductance spectra by spline interpolation. Next, a background subtraction is performed to isolate the Kondo resonance features as frequently applied in literature^{17,52,53}. The background is modeled as a linear function⁵³ connecting two reference points at $V = -10$ mV and $V = 0$ V. Using the background subtracted spectra (e.g., Fig. 2c), two local maxima are identified, allowing the extraction of their energy separation Δ_h and the corresponding peak heights H_1 and H_2 .

7. Tight-binding model of UTe₂

The parameters used to calculate the differential conductance dI/dV are estimated from a tight-binding (TB) model of UTe₂ previously proposed⁵⁴. Specifically, we consider the limits where the localized U-5*f* states are primarily coupled with either U-6*d* electrons (magnetic field along the *a*-axis; $\theta = 0$) or Te-5*p* electrons (magnetic field perpendicular to *a* axis; $\theta = \pi/2$) so that the hybridization between U-6*d* and Te-5*p* states is assumed to be negligible. The non-interacting U-6*d* electrons are described by

$$H_{U-6d}(k_x, k_y, k_z) = \begin{pmatrix} \mu_U - 2t_U \cos k_x - 2t_{ch,U} \cos k_y & -\Delta_U - 2t'_U \cos k_x - 2t'_{ch,U} \cos k_y - 4t_{z,U} e^{-i\frac{k_z}{2}} \cos \frac{k_x}{2} \cos \frac{k_y}{2} \\ -\Delta_U - 2t'_U \cos k_x - 2t'_{ch,U} \cos k_y - 4t_{z,U} e^{i\frac{k_z}{2}} \cos \frac{k_x}{2} \cos \frac{k_y}{2} & \mu_U - 2t_U \cos k_x - 2t_{ch,U} \cos k_y \end{pmatrix}$$

expressed in the basis of two U atoms that form the uranium dimer in the center of the unit cell. Here, μ_U is the chemical potential, t_U, t'_U are the hopping along the *a*-axis and between U-atoms, $t_{ch,U}, t'_{ch,U}$ are hopping between U chains in the *a-b* plane, $t_{z,U}$ is the hopping along the *c*-axis, Δ_U is the intradimer overlap respectively. The non-interacting Te-5*p* electrons is obtained by

$$H_{Te-5p}(k_x, k_y, k_z) = \begin{pmatrix} \mu_{Te} - 2t_{ch,Te} \cos k_x & -\Delta_{Te} - 2t_{Te} e^{-ik_y} - 2t_{z,Te} \cos \frac{k_x}{2} \cos \frac{k_y}{2} \cos \frac{k_z}{2} \\ -\Delta_{Te} - 2t_{Te} e^{ik_y} - 2t_{z,Te} \cos \frac{k_x}{2} \cos \frac{k_y}{2} \cos \frac{k_z}{2} & \mu_{Te} - 2t_{ch,Te} \cos k_x \end{pmatrix}$$

expressed in the basis of the two Te sublattice sites along the Te chain directions. Here, μ_{Te} is the chemical potential, Δ_{Te} is the intra-unit cell overlap between two Te atoms. Finally, t_{Te} and $t_{ch,Te}(t_{z,Te})$ are the nearest-neighbor hopping integrals within a Te chain along *b* direction and between neighboring Te chains along *a* direction (*c* direction), respectively. All parameters in H_{U-6d} and H_{Te-5p} are adapted from Ref. 54.

8. Kondo resonance model of UTe₂

We employ a minimal model H_{total} for the Kondo resonance in UTe₂ that encodes our hypothesis of a switch of primary Kondo hybridization channels driven by magnetic field direction: When the external magnetic field is along the *a*-axis ($\theta = 0$), the CDW is suppressed so that U-6*d* electrons are the main participants due to their vicinity to the localized U-5*f* states. When the external magnetic field is perpendicular to the *a*-axis ($\theta = \frac{\pi}{2}$), the U-6*d* electrons contribute less to the Kondo resonance due to the formation of CDW, and the main participating conduction electrons in the Kondo resonance become the Te-5*p* electrons due to their availability.

In the following, we will first describe the calculation of differential tunneling conductance dI/dV using H_{total} in two limiting cases: the case where the in-plane magnetic field $\mathbf{B}_{\parallel} \perp a$ -axis ($\theta = \pi/2$ in Fig. 4e) and the case where $\mathbf{B}_{\parallel} \parallel a$ -axis ($\theta = 0$ in Fig. 4f), where the localized U-5f states dominantly hybridized with Te-5p and U-6d orbitals, respectively. The total Hamiltonian is given by

$$H_{\text{total}} = H_{\text{UTe}_2} + H_{\text{tip}} + H_{\text{UTe}_2\text{-tip}}$$

In H_{UTe_2} , we retain only the conduction electron states relevant to the Kondo resonance: the conduction channel is dominated by U-6d states at $\theta = 0$ and by Te-5p states at $\theta = \pi/2$. The Kondo lattice Hamiltonian is given by

$$H_{\text{UTe}_2} = \sum_{\mathbf{k}\sigma} \epsilon_{\mathbf{k}} c_{\mathbf{k}\sigma}^{\dagger} c_{\mathbf{k}\sigma} + J \sum_{\mathbf{i}} \mathbf{S}_{\mathbf{i}} \cdot \left(\sum_{\alpha\beta} c_{\mathbf{i}\alpha}^{\dagger} \boldsymbol{\sigma}_{\alpha\beta} c_{\mathbf{i}\beta} \right)$$

where J is the Kondo-coupling strength, $c_{\mathbf{k}\sigma}^{\dagger}$ creates the conduction electron state with momentum \mathbf{k} and spin σ , and $\mathbf{S}_{\mathbf{i}}$ is the spin operator of localized U-5f states at site \mathbf{i} . The non-interacting dispersion, $\epsilon_{\mathbf{k}}$ is obtained by diagonalizing the TB model of UTe₂ described in the previous section, i.e. the eigenvalues of U-6d matrix when $\theta = 0$, and of Te-5p orbitals when $\theta = \pi/2$. Within the mean-field framework (e.g. in Ref. 55), the Kondo coupling in H_{UTe_2} is approximated by introducing the pseudo-fermions, $\mathbf{S}_{\mathbf{i}} = \sum_{\alpha\beta} f_{\mathbf{i}\alpha}^{\dagger} \boldsymbol{\sigma}_{\alpha\beta} f_{\mathbf{i}\beta}$,

$$H_{\text{UTe}_2} \approx \sum_{\mathbf{k}\sigma} \epsilon_{\mathbf{k}} c_{\mathbf{k}\sigma}^{\dagger} c_{\mathbf{k}\sigma} + v \sum_{\mathbf{i}\sigma} (c_{\mathbf{i}\sigma}^{\dagger} f_{\mathbf{i}\sigma} + \text{H. c.}) + \epsilon_f \sum_{\mathbf{i}\sigma} f_{\mathbf{i}\sigma}^{\dagger} f_{\mathbf{i}\sigma}$$

where $v = -J \langle f_{\mathbf{i}\sigma}^{\dagger} c_{\mathbf{i}\sigma} \rangle$ is the hybridization amplitude, and the energy of localized states ϵ_f sets the center of Kondo resonance. The Hamiltonian of STM tip electrons H_{tip} is given by

$$H_{\text{tip}} = \sum_{\mathbf{k}\sigma} \epsilon_{\mathbf{k}} a_{\mathbf{k}\sigma}^{\dagger} a_{\mathbf{k}\sigma}$$

Finally, the tunneling between the tip and sample is described by

$$H_{\text{UTe}_2\text{-tip}} = \sum_{\sigma} a_{i_0\sigma}^{\dagger} (t_f f_{i_0\sigma} + t_c c_{i_0\sigma}) + \text{H. c.}$$

where i_0 is the tip position, and t_f and t_c are the tunneling strengths between the STM tip to the localized and conduction electrons, respectively.

The dI/dV for model H_{total} is given by³⁵

$$\frac{dI}{dV}(\omega = eV - i\Gamma) \propto t_c^2 \frac{1}{D_c} \text{Im} \left[\left(\frac{\tilde{q}}{v} \right)^2 \frac{D_c}{\omega - \epsilon_f} + \left(1 + \frac{\tilde{q}}{\omega - \epsilon_f} \right)^2 \log \left(\frac{\omega + D_1 - \frac{v^2}{\omega - \epsilon_f}}{\omega - D_2 - \frac{v^2}{\omega - \epsilon_f}} \right) \right]$$

where Γ is the disorder broadening, and $\tilde{q} \propto \frac{vt_f}{Jt_c}$ captures the ratio between the tunneling channels and determines the asymmetry of Fano line shape. Here, we treat \tilde{q} as an effective parameter

constrained by physically reasonable values for each field direction θ . Moreover, $-D_1$ and D_2 denote the lower and top band edges measured from the chemical potential and $D_c = D_1 + D_2$ is the bandwidth whose inverse is proportional to the density of state. In this analytic form, \tilde{q}, v, t_c are treated as control parameters constrained within physically reasonable ranges and determined by fitting to the experimental data. We then obtain the parameters D_1 and D_2 for U-6d and Te-5p electrons from the tight-binding models H_{U-6d} and H_{Te-5p} given in the previous section, respectively.

The dependence of $dI/dV(\theta)$ on the external magnetic field direction θ is controlled by the variable set $(D_1, D_2, \tilde{q}, v, t_c)$. The values of these variables are determined by the conduction channel that participates in Kondo resonance: At $\theta = 0$, we set $(D_1, D_2, \tilde{q}, v, t_c)$ to take the values for U-6d electrons, estimated from H_{U-6d} . At $\theta = \frac{\pi}{2}$, we set $(D_1, D_2, \tilde{q}, v, t_c)$ to take the values for Te-5p electrons, estimated from H_{Te-5p} . In contrast, (t_f, ϵ_f) is set by the localized U-5f states and is independent of the field direction. We choose $v_d > v_p$ since the hybridization strength between U-5f and U-6d states is expected stronger than that between U-5f and Te-5p states due to proximity. Meanwhile, we set the tunneling strengths from the STM tip to the U-6d and Te-5p conduction electrons to be $t_d < t_p$ since the Te-5p electrons are spatially closer to the tip on the (011) surface (Figs. 4e,f). The specific values of TB and fitting parameters used in Fig. 4g at $\theta = 0$ and $\pi/2$ are $t_U = 150, t'_U = 80, t_{ch,U} = 10, t'_{ch,U} = 0, t_{z,U} = -30, \Delta_U = 400, t_{Te} = -1500, t_{ch,Te} = 0, t_{z,Te} = -50, \Delta_{Te} = -1500$, fitted from density functional theory and taken from Ref. 54. The other fitting parameters are taken to be $\mu_U = 200, \mu_{Te} = -2000, \epsilon_f = -3, \tilde{q}_d = 500, \tilde{q}_p = 300, v_d = 40, v_p = 35, t_d = 1.5, t_p = 3.5, \Gamma = 0.7$, where all units are in meV.

For intermediate orientation $0 < \theta < \pi/2$, we retain the same analytical form of dI/dV and calculate the θ -dependence by interpolating the model parameters between these two limits. For example, we parametrize the tunneling strength between the tip and conduction electrons as $t_c(\theta) = t_d \left(1 - \frac{\theta}{\pi/2}\right) + t_p \frac{\theta}{\pi/2}$, where $t_c(\theta = 0) = t_d$ and $t_c(\theta = \pi/2) = t_p$. Other variables D_1, D_2, \tilde{q} , and v , are interpolated in a similar way for $0 < \theta < \pi/2$.

Acknowledgements

The authors thank D. Morr, H. Pirie, B. Janko, B. Assaf, E. Huang, and Q. Gu for valuable discussions. Experimental STM investigations were supported by the U.S. Department of Energy (DOE), Office of Science, Office of Basic Energy Sciences under Award Numbers DE-SC0025021. Theoretical modeling was supported by the National Science Foundation Grant No. DMR-2238748. N.S. and M.T. acknowledge support from the Notre Dame Materials Science and Engineering Fellowship. UTe₂ crystal synthesis at the Los Alamos National Laboratory was supported by the U.S. Department of Energy, Office of Basic Energy Sciences, Division of Materials Science and Engineering under project ‘‘Quantum Fluctuations in Narrow-Band

Systems.” M.M.B. acknowledges support from the Los Alamos Laboratory Directed Research and Development program.

Author contributions

X.L. conceived the project. N.S., M.T., and J.M. performed the measurements. M.M.B, S.M.T., and P.F.S.R. synthesized the crystals. Y.-T.H. and H.J.Y. performed theoretical and numerical modeling. N.S., F.C., M.T., and J.M. performed data analysis. X.L. wrote the manuscript with input from all authors. All authors contributed to data interpretation.

Data availability

All data needed to evaluate the conclusions in the paper are present in the paper and/or the Supplementary Information. Additional data related to this paper may be requested from the authors.

Code availability

Gwyddion and MATLAB are used for data analysis. The code is available from the corresponding authors on reasonable request.

Competing financial interests

The authors declare no competing financial interests.

Figures

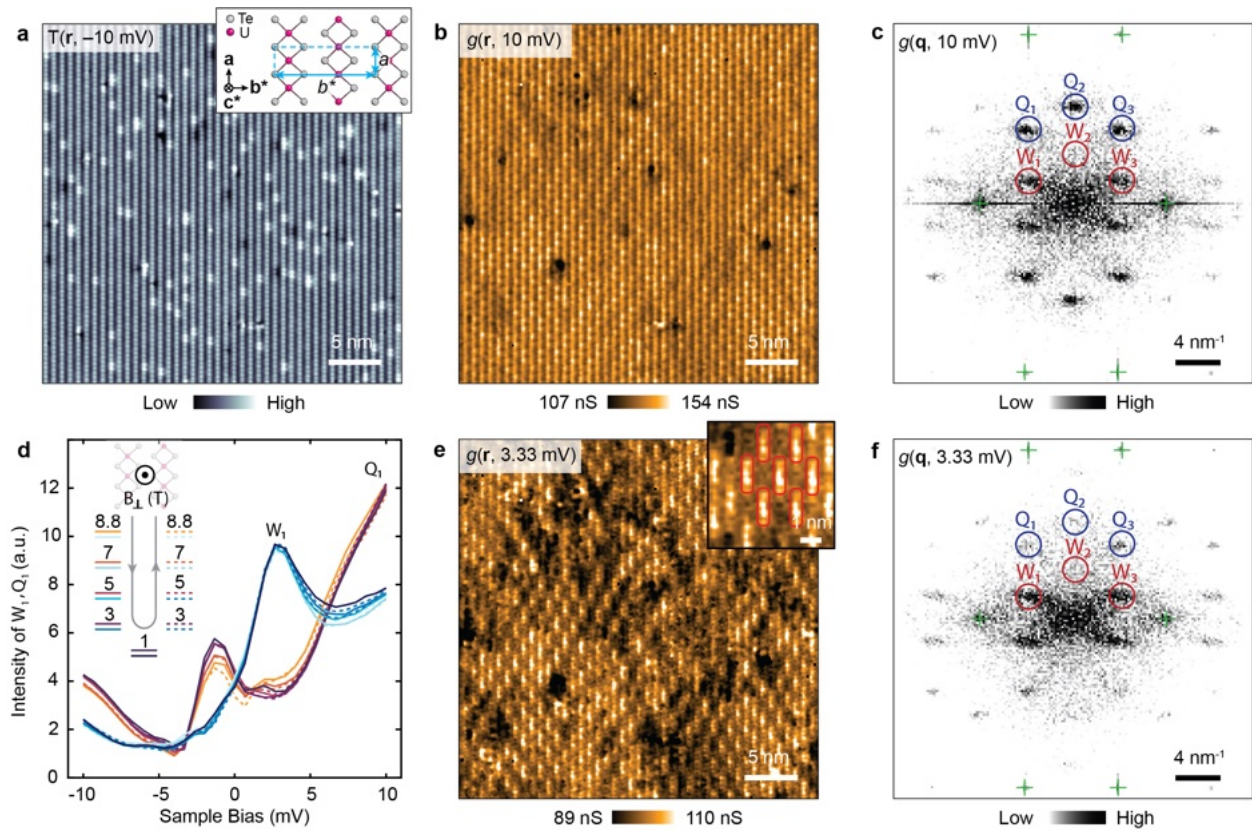


Figure 1. Discovery of a new staggered CDW

a, STM topographic image of UTe_2 (011) surface ($V_b = -10$ mV, $I_t = 1$ nA). Inset: schematic of the UTe_2 (011) surface structure. **b**, Differential conductance image $g(\mathbf{r}, 10$ mV) in the same field of view as in (a) and **c**, its Fourier transform, acquired at 0.3 K. The Bragg peaks are indicated by green crosses, and the CDW wavevectors are indicated by blue (Q_i) and red (W_i) circles. At this bias, the Q_i CDW has maximal intensity. **d**, Bias-dependence of the CDW intensity at different B_{\perp} and field-sweeping directions. **e**, Differential conductance image $g(\mathbf{r}, 3.33$ mV) in the same field of view as in (a) and **f**, its Fourier transform. The Bragg peaks are indicated by green crosses, and the CDW wavevectors are indicated by blue (Q_i) and red (W_i) circles.

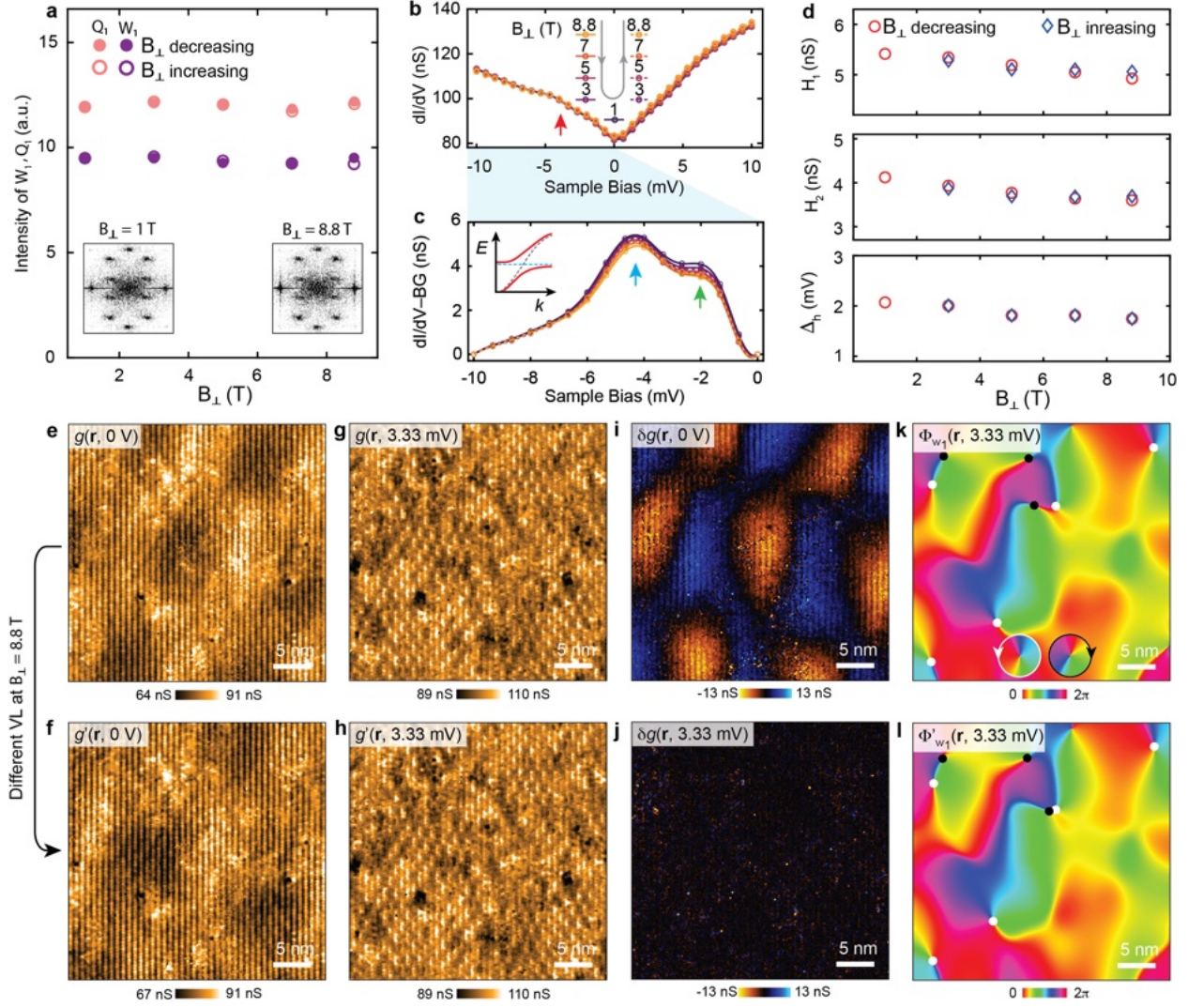


Figure 2. Insensitivity of CDW and Kondo resonance to B_{\perp}

a, Nearly unchanged extracted intensity of W_1 and Q_1 as a function of B_{\perp} . Inset: $g(\mathbf{q}, 10 \text{ mV})$ images showing minimal differences between $B_{\perp} = 1 \text{ T}$ and 8.8 T . **b**, A series of dI/dV spectra taken at 0.3 K under various B_{\perp} and field ramping directions. **c**, Background-subtracted spectra (see Methods) in the negative energy range, showing the presence of two peaks indicated by the blue and green arrows. Inset: schematic of the hybridization between a light conduction band (grey) and a heavy f -electron band (blue) in a Kondo lattice. **d**, Extracted peak heights $H_{1,2}$, corresponding to the peaks indicated by the blue and green arrows in (c), respectively, and the hybridization gap Δ_h , defined as the energy separation of the two peaks, as a function of B_{\perp} and field ramping directions. **e,f**, Differential conductance images of the same field of view after two separate field cooling procedures (labeled as $g(\mathbf{q}, 0 \text{ V})$ and $g'(\mathbf{q}, 0 \text{ V})$) under $B_{\perp} = 8.8 \text{ T}$, showing two displaced triangular VLs. **g,h**, Corresponding $g(\mathbf{q}, 3.33 \text{ mV})$ and $g'(\mathbf{q}, 3.33 \text{ mV})$ images showing virtually no differences, acquired simultaneously and in the same field of view as (e,f). **i,h**, Difference images and

$\delta g(\mathbf{r}, V) \equiv g(\mathbf{r}, V) - g'(\mathbf{r}, V)$ calculated at $V = 0$ and 3.33 mV, respectively. **k,l**, Spatial phases Φ_{W_1} and Φ'_{W_1} of the W_1 CDW extracted in the same field view as (e,f) with topological defects in the form vortices and anti-vortices indicated by white and black dots, respectively. A pair of such defects is shown in the inset of (k).

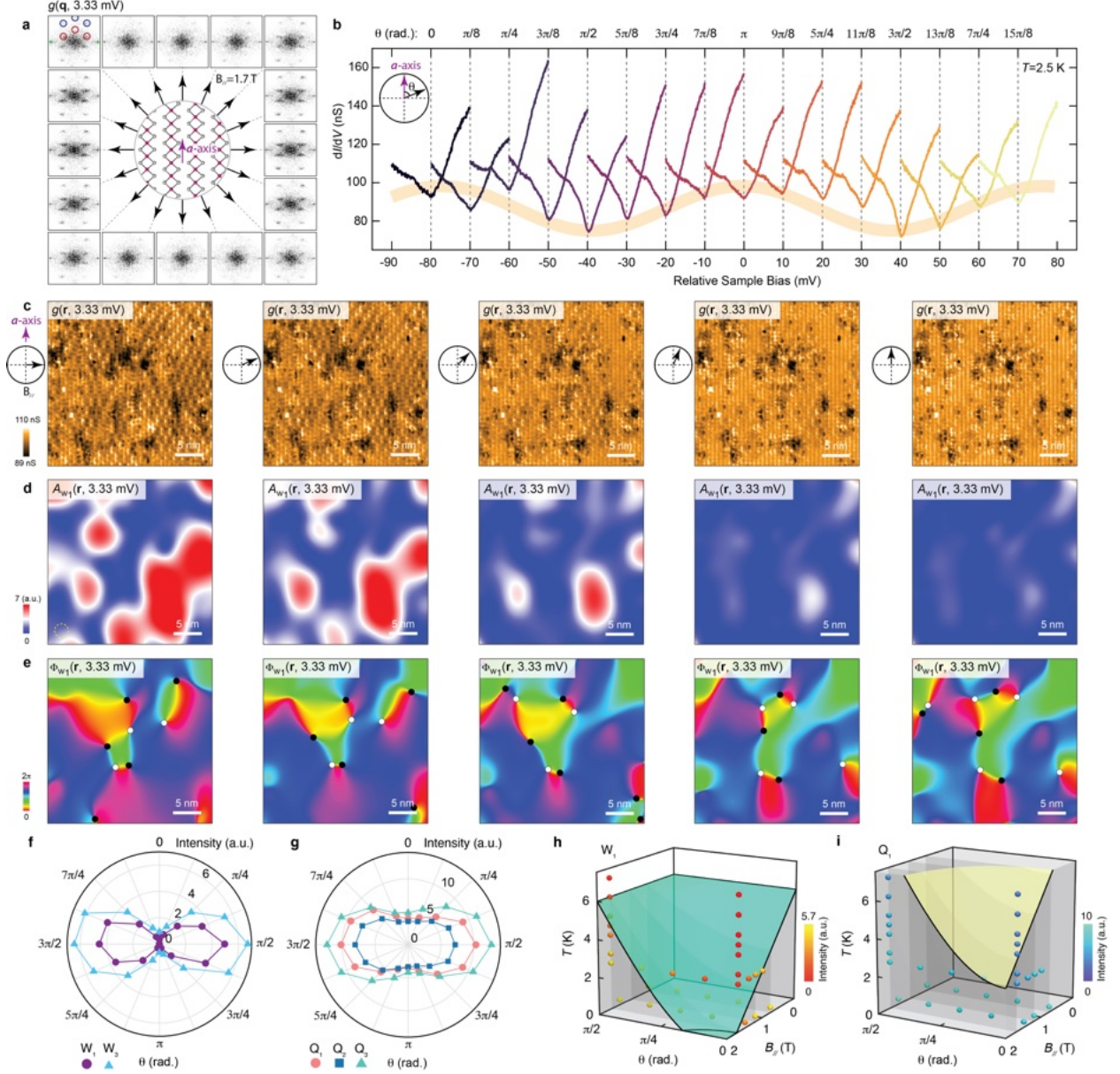


Figure 3 Vector magnetic field manipulation of CDW

a, A series of $g(\mathbf{q}, 3.33 \text{ mV})$ images acquired at 2.5 K and under a fixed $B_{\perp} = 1 \text{ T}$, which has virtually no effect on the CDW, and $B_{\parallel} = 1.7 \text{ T}$ applied along different in-plane directions as indicated by the black arrows. The W_i and Q_i CDW peaks are indicated by the red and blue circles, respectively. **b**, A series of dI/dV spectra taken when the angle θ between \mathbf{B}_{\parallel} and the a -axis of UTe_2 is varied between 0 and 2π . The periodic modulation of the zero bias conductance is indicated by the thick orange curve. **c**, Real space images of $g(\mathbf{r}, 3.33 \text{ mV})$, **d**, the amplitude of W_1 modulation $A_{W_1}(\mathbf{r}, 3.33 \text{ mV})$, and **e**, the spatial phase of W_1 modulation $\Phi_{W_1}(\mathbf{r}, 3.33 \text{ mV})$ for $\theta = \frac{\pi}{2}, \frac{3\pi}{8}, \frac{\pi}{4},$ and $\frac{\pi}{8}$. The topological defects in Φ_{W_1} are indicated by the white and black dots. The real space Gaussian window size (see Methods) is indicated by the

dashed circle in the left panel. **f**, Extracted integrated intensity of the W_i and **g**, Q_i CDW peaks as a function of θ from $g(\mathbf{q}, 3.33 \text{ mV})$ and $g(\mathbf{q}, 10 \text{ mV})$, respectively, showing clear in-plane anisotropy. **h**, Color-coded intensity of W_1 and **i**, Q_1 CDWs plotted in the phase space of B_{\parallel} , θ , and T . The fitted phase boundaries defining the CDW states are colored green and yellow, respectively.

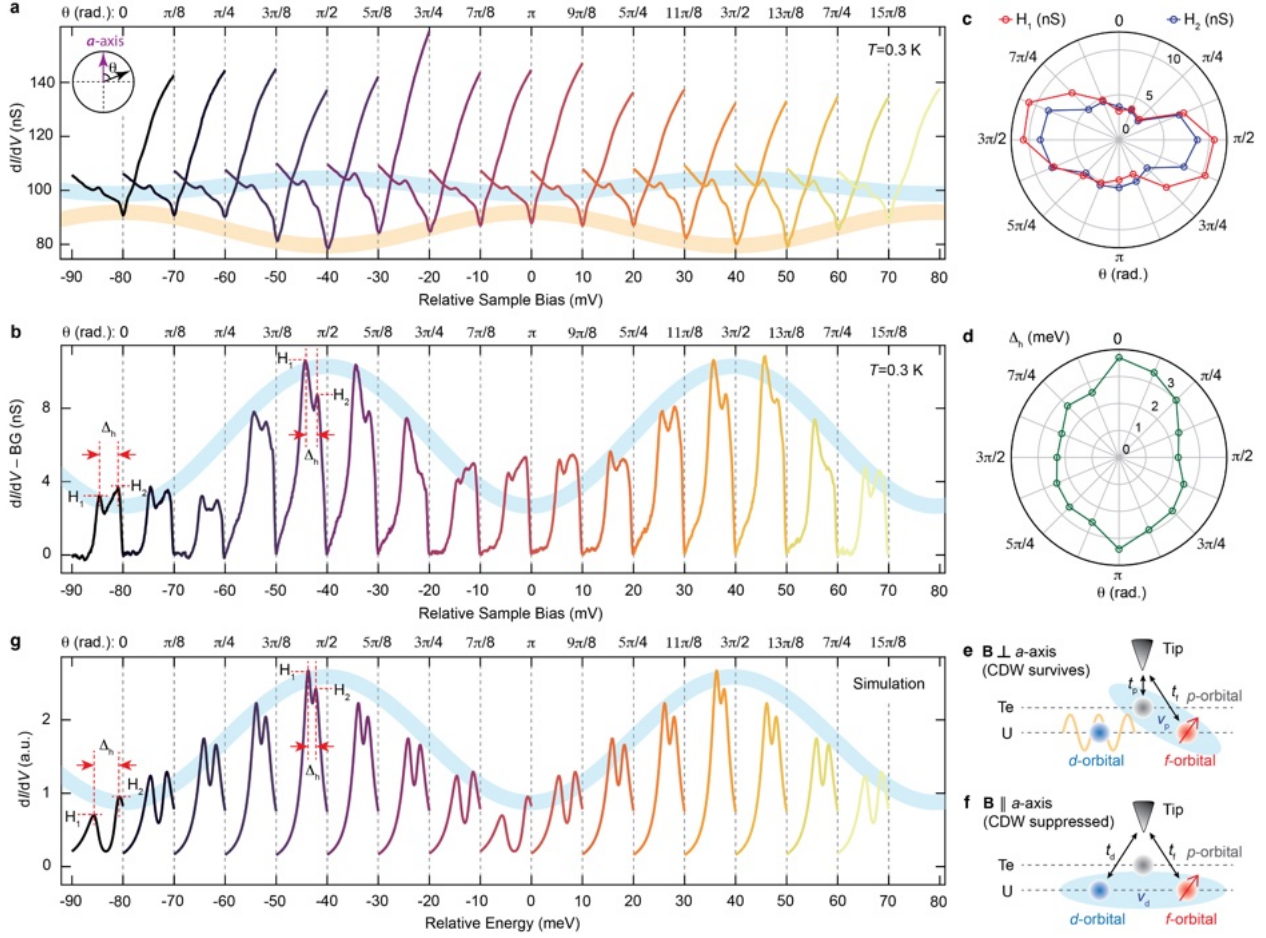


Figure 4 Vector magnetic field manipulation of Kondo effect

a, A series of dI/dV spectra taken at 0.3 K under $B_{\parallel} = 1.95$ T when the angle θ between B_{\parallel} and the a -axis of UTe_2 is varied between 0 and 2π . The periodic modulation of the zero bias conductance is indicated by the thick orange curve. An anti-correlated modulation of the Kondo resonance feature is indicated by the thick blue curve. **b**, Corresponding background-subtracted spectra of (a), highlighting the modulation of the Kondo resonance. The peak heights ($H_{1,2}$) and hybridization gap (Δ_h) are indicated at $\theta = 0$ and $\pi/2$. **c**, Extracted angular dependence of $H_{1,2}$ and **d**, Δ_h , showing clear anisotropy and anti-correlation. **e**, When the in-plane field $B_{\parallel} \perp a$ -axis ($\theta = \pi/2$), the U-6d orbital states develop CDW order and the effective Kondo hybridization (blue oval) is in the p - f channel and probed by an STM tip. **f**, When $B_{\parallel} \parallel a$ -axis ($\theta = 0$), the CDW order in U-6d orbital states is suppressed and the effective Kondo hybridization is in the d - f channel and probed by an STM tip. Here, t_p , t_d and t_f are the tunneling strengths between the STM tip to the Te-5p, U-6d, and U-5f electrons, respectively; v_p and v_d are the hybridization amplitudes of U-5f with Te-5p and U-6d, respectively. **g**, A series of calculated dI/dV spectra as θ evolves, reproducing qualitatively the experimental

dI/dV spectra in (b). The calculation details and tight-binding model parameters of U-6*d* and Te-5*p* orbitals are given in the Methods section.

References

- 1 Fradkin, E., Kivelson, S. A. & Tranquada, J. M. Colloquium: Theory of intertwined orders in high temperature superconductors. *Rev. Mod. Phys.* **87**, 457-482 (2015).
- 2 Lee, P. A., Nagaosa, N. & Wen, X. G. Doping a Mott insulator: physics of high-temperature superconductivity. *Rev. Mod. Phys.* **78**, 17-85 (2006).
- 3 Keimer, B., Kivelson, S. A., Norman, M. R., Uchida, S. & Zaanen, J. From quantum matter to high-temperature superconductivity in copper oxides. *Nature* **518**, 179-186 (2015).
- 4 Kivelson, S. A. et al. How to detect fluctuating stripes in the high-temperature superconductors. *Rev. Mod. Phys.* **75**, 1201 (2003).
- 5 Comin, R. & Damascelli, A. Resonant X-ray scattering studies of charge order in cuprates. *Annu. Rev. Condens. Matter Phys.* **7**, 369-405 (2016).
- 6 Aoki, D. et al. Unconventional superconductivity in heavy fermion UTe_2 . *J. Phys. Soc. Jpn.* **88**, 043702 (2019).
- 7 Ran, S. et al. Nearly ferromagnetic spin-triplet superconductivity. *Science* **365**, 684-687 (2019).
- 8 Lewin, S. K., Frank, C. E., Ran, S., Paglione, J. & Butch, N. P. A review of UTe_2 at high magnetic fields. *Rep. Prog. Phys.* **86**, 114501 (2023).
- 9 Sharma, N. et al. Observation of persistent zero modes and superconducting vortex doublets in UTe_2 . *ACS Nano* **19**, 31539-31550 (2025).
- 10 Yang, Z. et al. Spectroscopic evidence of symmetry breaking in the superconducting vortices of UTe_2 . *Natl. Sci. Rev.* **12**, nwaf267 (2025).
- 11 Yin, R. et al. Yin-Yang vortex on UTe_2 (011) surface. Preprint at <https://arxiv.org/abs/2503.21506> (2025).
- 12 Duan, C. et al. Resonance from antiferromagnetic spin fluctuations for superconductivity in UTe_2 . *Nature* **600**, 636-640 (2021).
- 13 Aishwarya, A. et al. Magnetic-field-sensitive charge density waves in the superconductor UTe_2 . *Nature* **618**, 928-933 (2023).
- 14 Gu, Q. et al. Detection of a pair density wave state in UTe_2 . *Nature* **618**, 921-927 (2023).
- 15 Aishwarya, A. et al. Melting of the charge density wave by generation of pairs of topological defects in UTe_2 . *Nat. Phys.* **20**, 964-969 (2024).
- 16 LaFleur, A. et al. Inhomogeneous high temperature melting and decoupling of charge density waves in spin-triplet superconductor UTe_2 . *Nat. Commun.* **15**, 4456 (2024).
- 17 Jiao, L. et al. Chiral superconductivity in heavy-fermion metal UTe_2 . *Nature* **579**, 523-527 (2020).
- 18 Li, P. et al. Charge density wave and weak Kondo effect in a Dirac semimetal $CeSbTe$. *Sci. China-Phys. Mech. Astron.* **64**, 237412 (2021).
- 19 Kang, B., Choi, S. & Kim, H. Orbital selective Kondo effect in heavy fermion superconductor UTe_2 . *npj Quantum Mater.* **7**, 64 (2022).

-
- 20 Miao, L. et al. Low energy band structure and symmetries of UTe_2 from angle-resolved photoemission spectroscopy. *Phys. Rev. Lett.* **124**, 076401 (2020).
- 21 Dieterich, W. & Fulde, P. Magnetic field dependence of the Peierls instability in one-dimensional conductors. *Z. Physik* **265**, 239-243 (1973).
- 22 Graf, D. et al. Suppression of a charge-density-wave ground state in high magnetic fields: spin and orbital mechanisms. *Phys. Rev. B* **69**, 125113 (2004).
- 23 Dupuis, N. & Montambaux, G. Localization and magnetic field in a quasi-one-dimensional conductor. *Phys. Rev. B* **46**, 9603 (1992).
- 24 Balseiro, C. A. & Falicov, L. M. Density waves in high magnetic fields: a metal-insulator transition. *Phys. Rev. Lett.* **55**, 2336 (1985).
- 25 Xu, X. et al. Directional field-induced metallization of quasi-one-dimensional $\text{Li}_{0.9}\text{Mo}_6\text{O}_{17}$. *Phys. Rev. Lett.* **102**, 206602 (2009).
- 26 Andres, D. et al. Orbital effect of a magnetic field on the low-temperature state in the organic metal α -(BEDT-TTF) $_2$ KHg(SCN) $_4$. *Phys. Rev. B* **64**, 161104 (2001).
- 27 Trontl, V. M. et al. Interplay of Kondo physics with incommensurate charge density waves in CeTe_3 . Preprint at <https://arxiv.org/abs/2502.04814> (2025).
- 28 Carpinelli, J. M., Weitering, H. H., Plummer, E. W. & Stumpf, R. Direct observation of a surface charge density wave. *Nature* **381**, 398-400 (1996).
- 29 Spera, M. et al. Insight into the charge density wave gap from contrast inversion in topographic STM images. *Phys. Rev. Lett.* **125**, 267603 (2020).
- 30 Pouget, J. P. The Peierls instability and charge density wave in one-dimensional electronic conductors. *C. R. Physique* **17**, 332-356 (2016).
- 31 Šaub, K., Barišić, S. & Friedel, J. Charge density wave Madelung constant in a system of linear chains. *Phys. Lett. A* **56**, 302-304 (1976).
- 32 Wang, S. et al. Odd-parity quasiparticle interference in the superconductive surface state of UTe_2 . *Nat. Phys.* **21**, 1555-1562 (2025).
- 33 Brooks, J. S. Magnetic field dependent and induced ground states in organic conductors. *Rep. Prog. Phys.* **71**, 126501 (2008).
- 34 Talavera, P. G. et al. Surface charge density wave in UTe_2 . Preprint at <https://arxiv.org/abs/2504.12505> (2025).
- 35 Maltseva, M., Dzero, M. & Coleman, P. Electron cotunneling into a Kondo lattice. *Phys. Rev. Lett.* **103**, 206402 (2009).
- 36 Park, W. K. et al. Observation of the hybridization gap and Fano resonance in the Kondo lattice URu_2Si_2 . *Phys. Rev. Lett.* **108**, 246403 (2012).
- 37 Seiro, S. et al. Evolution of the Kondo lattice and non-Fermi liquid excitations in a heavy-fermion metal. *Nat. Commun.* **9**, 3324 (2018).
- 38 Jiao, L. et al. Additional energy scale in SmB_6 at low-temperature. *Nat. Commun.* **7**, 13762 (2016).
- 39 Liu, Y. et al. Pair density wave state in a monolayer high- T_c iron-based superconductor. *Nature* **618**, 934-939 (2023).

-
- 40 Zhang, K.-W. et al. Unveiling the charge density wave inhomogeneity and pseudogap state in $1T$ -TiSe₂. *Sci. Bull.* **63**, 426-432 (2018).
- 41 Snow, C. S., Karpus, J. F., Cooper, S. L., Kidd, T. E. & Chiang, T.-C. Quantum melting of the charge-density-wave state in $1T$ -TiSe₂. *Phys. Rev. Lett.* **91**, 136402 (2003).
- 42 Sacépé, B., Feigel'man, M. & Klapwijk, T. M. Quantum breakdown of superconductivity in low-dimensional materials. *Nat. Phys.* **16**, 734-746 (2020).
- 43 Rosa, P. F. et al. Single thermodynamic transition at 2 K in superconducting UTe₂ single crystals. *Commun. Mater.* **3**, 33 (2022).
- 44 McDonald, R. D. et al. Charge-density waves survive the Pauli paramagnetic limit. *Phys. Rev. Lett.* **93**, 076405 (2004).
- 45 Niu, Q. et al. Evidence of Fermi surface reconstruction at the metamagnetic transition of the strongly correlated superconductor UTe₂. *Phys. Rev. Research* **2**, 033179 (2020).
- 46 Niu, Q. et al. Fermi-surface instability in the heavy-fermion superconductor UTe₂. *Phys. Rev. Lett.* **124**, 086601 (2020).
- 47 Peters, R., Hoshino, S., Kawakami, N., Otsuki, J. & Kuramoto, Y. Charge order in Kondo lattice systems. *Phys. Rev. B* **87**, 165133 (2013).
- 48 Lawler, M. J. et al. Intra-unit-cell electronic nematicity of the high- T_c copper-oxide pseudogap states. *Nature* **466**, 347-351 (2010).
- 49 Carneiro, F. B. et al. Unveiling charge density wave quantum phase transitions by x-ray diffraction. *Phys. Rev. B* **101**, 195135 (2020).
- 50 Gruner, T. et al. Charge density wave quantum critical point with strong enhancement of superconductivity. *Nat. Phys.* **13**, 967-972 (2017).
- 51 Fang, A., Straquadine, J. A., Fisher, I. R., Kivelson, S. A. & Kapitulnik, A. Disorder-induced suppression of charge density wave order: STM study of Pd-intercalated ErTe₃. *Phys. Rev. B* **100**, 235446 (2019).
- 52 Moro-Lagares, M. et al. Real space manifestations of coherent screening in atomic scale Kondo lattices. *Nat. Commun.* **10**, 2211 (2019).
- 53 Fan, K. et al. Artificial superconducting Kondo lattice in a van der Waals heterostructure. *Nat. Commun.* **15**, 8797 (2024).
- 54 Theuss, F. et al. Single-component superconductivity in UTe₂ at ambient pressure. *Nat. Phys.* **20**, 1124-1130 (2024).
- 55 Millis, A. J. & Lee, P. A. Large-orbital-degeneracy expansion for the lattice Anderson model. *Phys. Rev. B* **35**, 3394 (1987).

Supplementary Information

Directional Manipulation of a Staggered Charge Density Wave and Kondo Resonance in UTe_2

Nileema Sharma^{1,2†}, Fangjun Cheng^{1,2†}, Hyeok Jun Yang^{1†}, Matthew Toole^{1,2}, James McKenzie^{1,2}, Mitchell M. Bordelon³, Sean M. Thomas³, Priscila F. S. Rosa³, Yi-Ting Hsu^{1*}, and Xiaolong Liu^{1,2*}

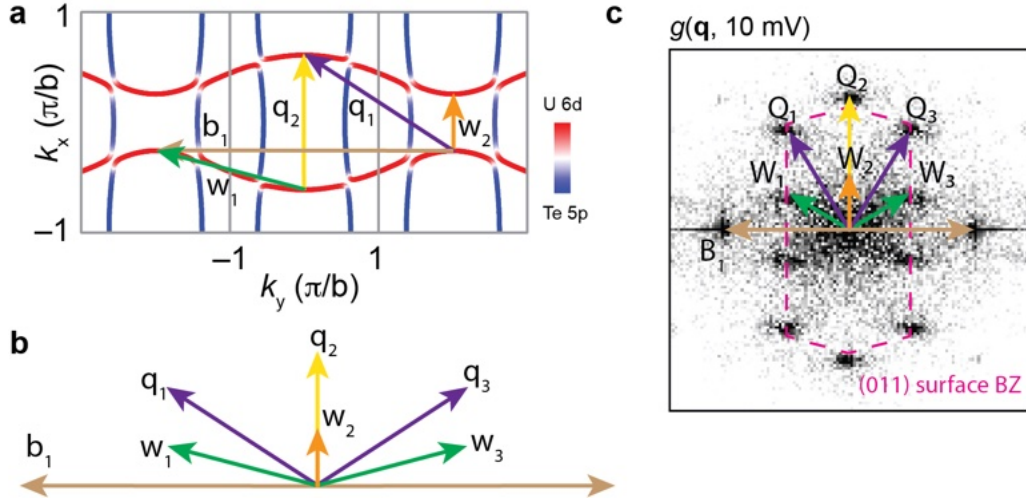
¹*Department of Physics and Astronomy, University of Notre Dame, Notre Dame, IN 46556, USA*

²*Stavropoulos Center for Complex Quantum Matter, University of Notre Dame, Notre Dame, IN 46556, USA*

³*Los Alamos National Laboratory, Los Alamos, New Mexico 87545, USA*

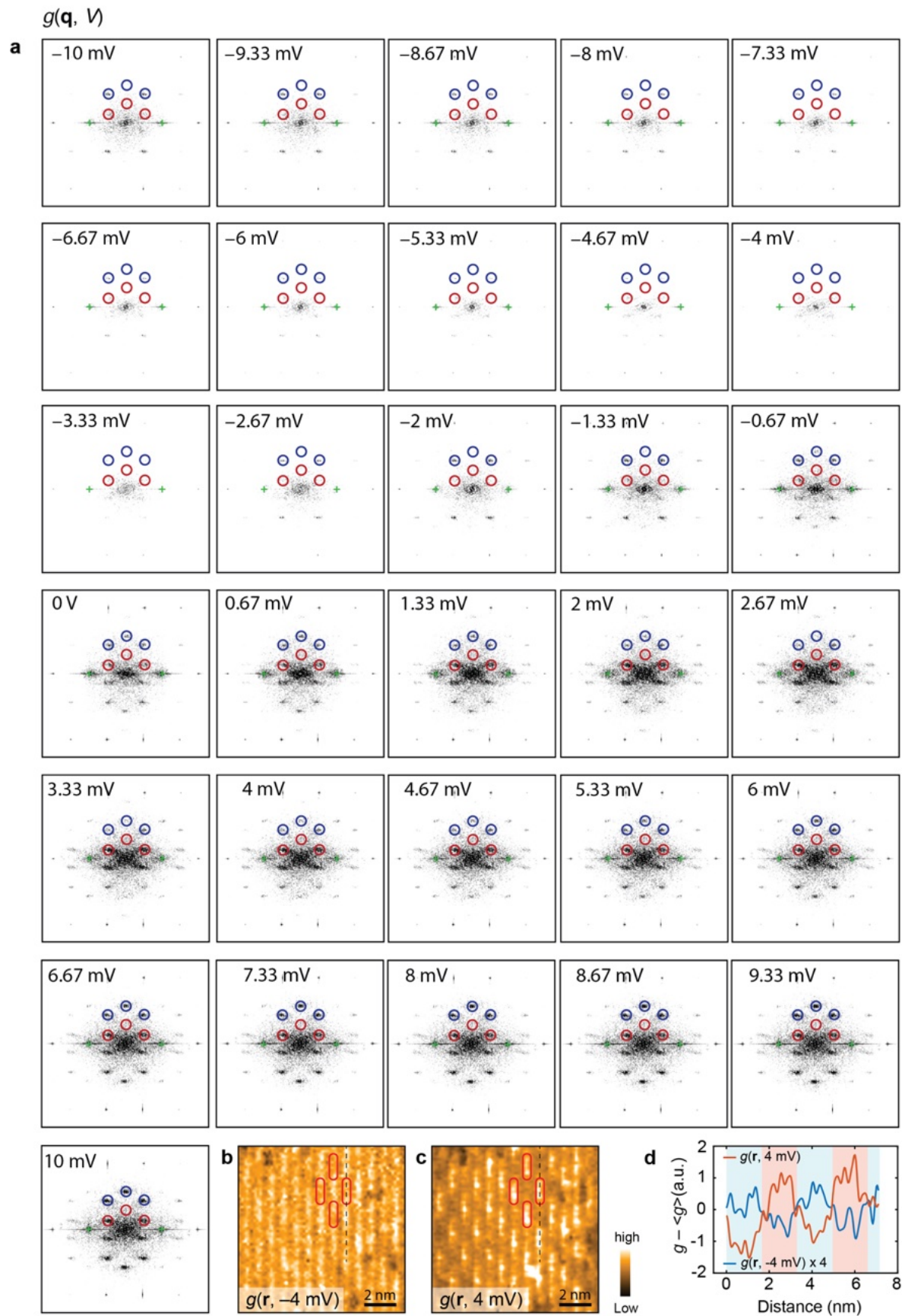
* Corresponding authors. yhsu2@nd.edu, xliu33@nd.edu

† These authors contributed equally to this work.



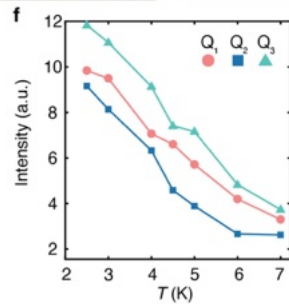
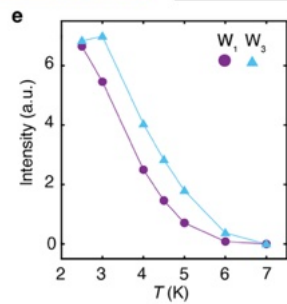
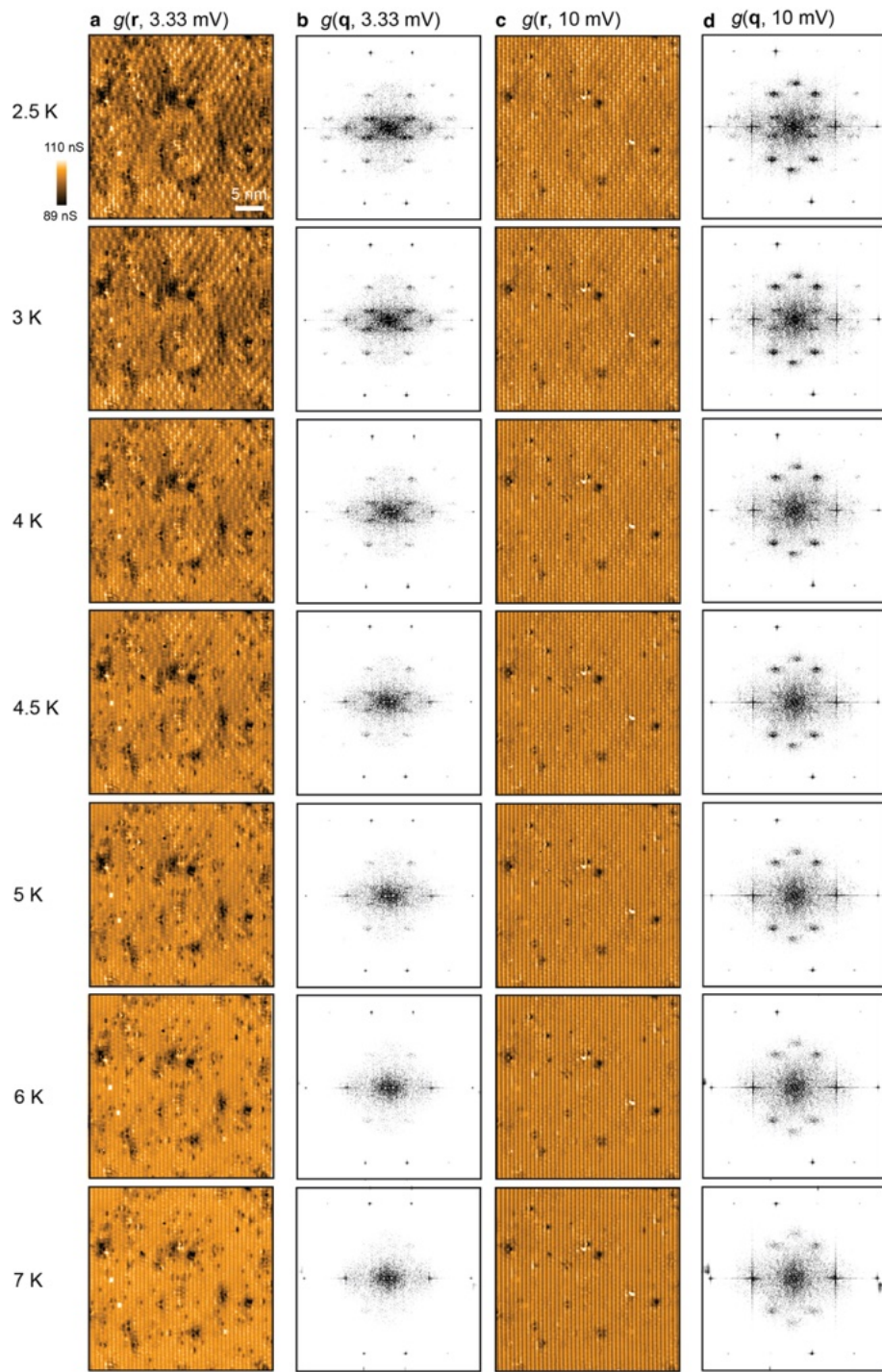
Supplementary Figure 1. Fermi surface and nesting vectors of UTe₂

a. Fermi surface (FS) of UTe₂ in the k_y (horizontal axis) – k_x (vertical axis) plane at $k_z = 0$, color coded to reflect the orbital contributions. The quasi-1D FSs primarily composed of U 6d and Te 5p orbitals run along k_y and k_x directions, respectively, and hybridize at their intersections. As identified in Ref. 32, the nesting vectors connect different portions of the FS involving only the U 6d orbitals (red). Among them, the b_1 vector is a Bragg vector. **b.** The same nesting vectors as in (a), but plotted with the origins together. **c.** Experimental $g(\mathbf{q}, 10 \text{ mV})$ image on the UTe₂ (011) surface with overlaid nesting vectors transformed to the (011) plane. To do so, we follow the same procedure demonstrated in ref. 32, where the transformation to the (011) plane corresponds to a change of y -axis coordinates as $Q_y = q_y \sin \theta$, where $\theta = 23.7^\circ$ is angle between the (011) surface normal and the b -axis. The resulting nesting wavevectors match closely the experimental ones. The (011) surface Brillouin zone (BZ) is shown in pink, constructed from the six Bragg vectors in Fig. 1c (green crosses).



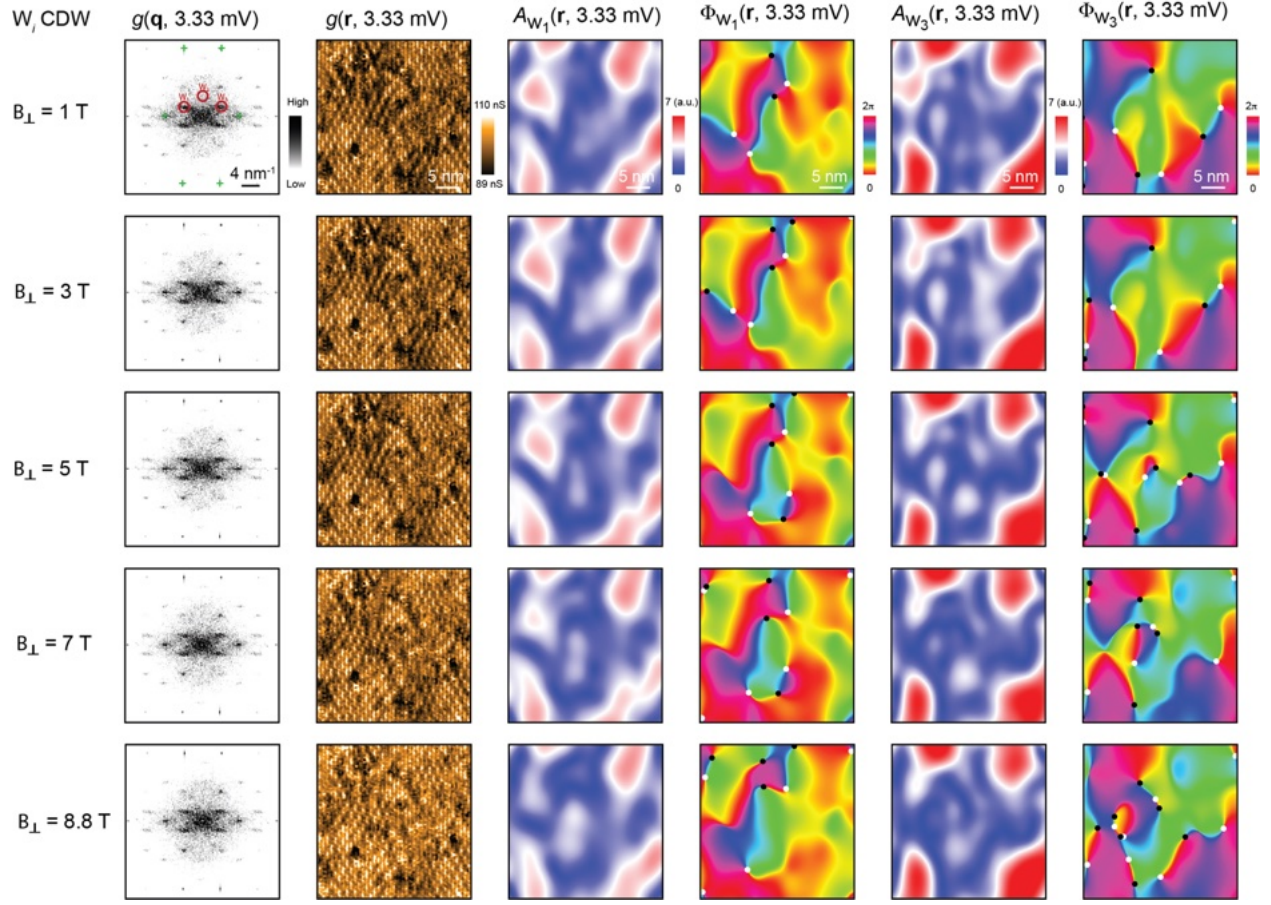
Supplementary Figure 2. Bias-dependence of CDWs and contrast inversion

a, A series of $g(\mathbf{q}, V)$ images in both the filled ($V < 0$) and empty states ($V > 0$) at 0.3 K. The CDWs are indicated by circles. **b**, $g(\mathbf{r}, -4 \text{ mV})$ and **c**, $g(\mathbf{r}, 4 \text{ mV})$ images in the same FOV, showing both the brick-wall-like pattern from the staggered W_i CDW, but with a contrast inversion. To better visualize this contrast inversion, we highlight four “bricks” in red. **d**, Line profiles of $g(\mathbf{r}, V) - \langle g(\mathbf{r}, V) \rangle$ along the dashed lines in (b,c), where $\langle g(\mathbf{r}, V) \rangle$ is the averaged differential conductance of the entire FOV. Contrast inversion in the filled and empty states are clearly seen, consistent with a CDW from Fermi surface nesting.



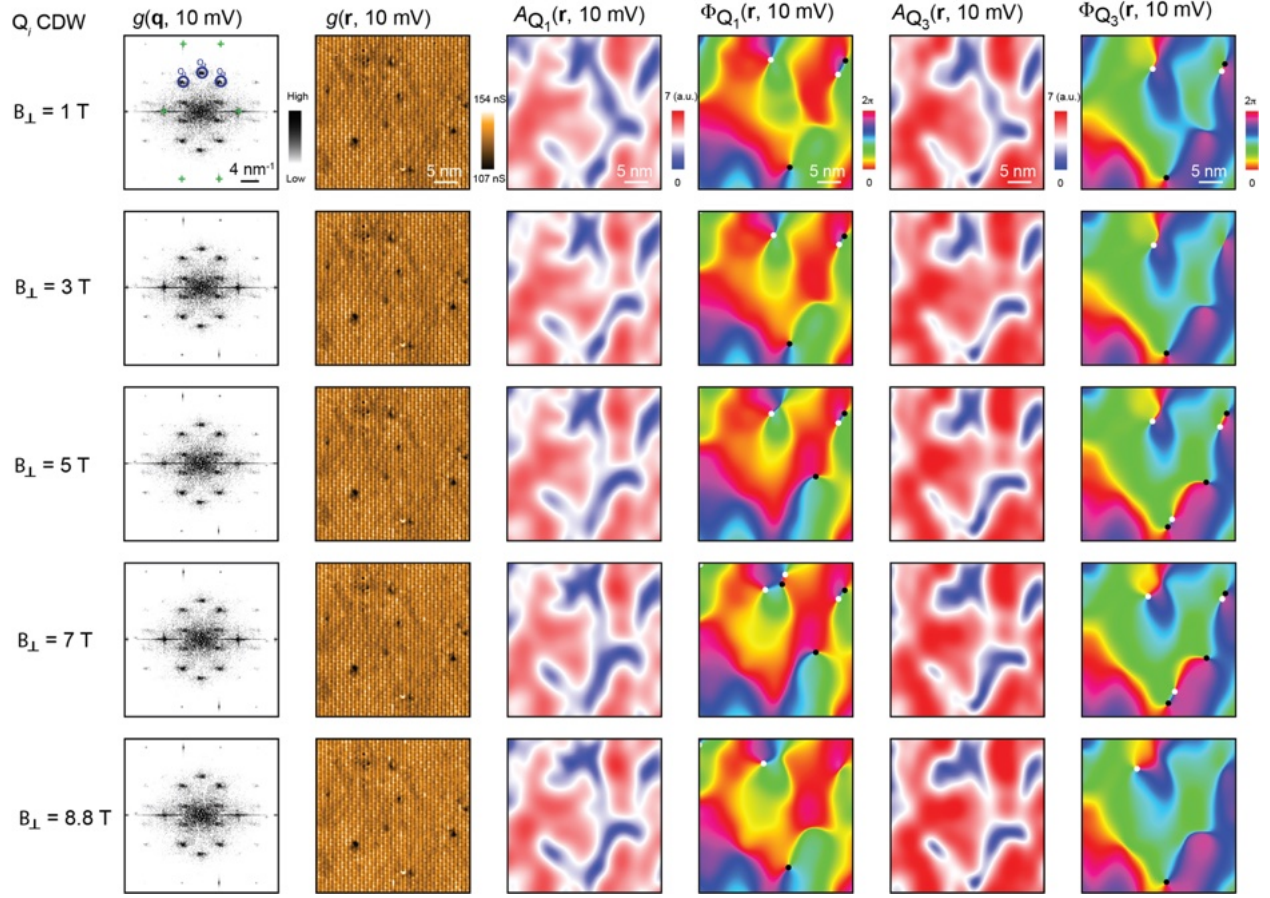
Supplementary Figure 3. Thermal melting of CDWs

a, A series of $g(\mathbf{r}, 3.33 \text{ mV})$, **b**, $g(\mathbf{q}, 3.33 \text{ mV})$, **c**, $g(\mathbf{r}, 10 \text{ mV})$, and **d**, $g(\mathbf{q}, 10 \text{ mV})$ images acquired in the same FOV at different temperatures, showing clearly the thermal melting of the W_i and Q_i CDWs. **e**, Intensity of the W_i and **f**, Q_i CDW (extracted from the FTs) as a function of temperature.



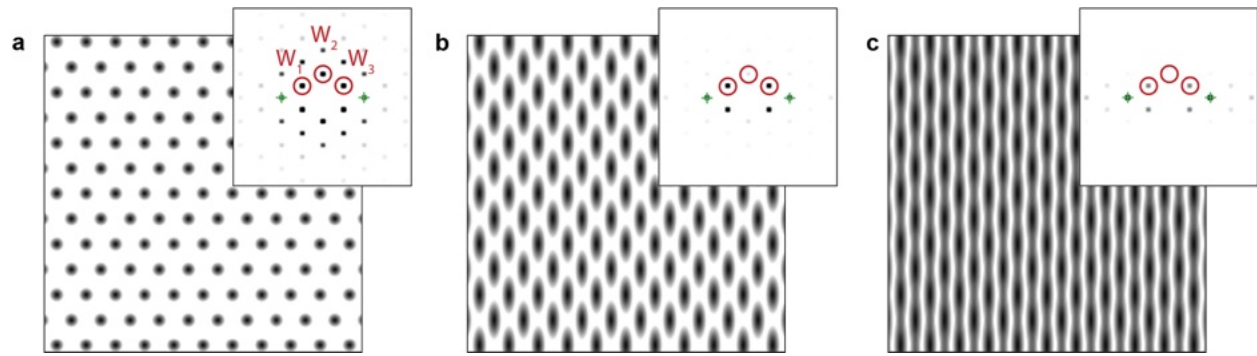
Supplementary Figure 4. Evolution of W_i CDW as a function of B_{\perp}

In the same FOV, the momentum-space ($g(\mathbf{q}, 3.33 \text{ mV})$) and real-space ($g(\mathbf{r}, 3.33 \text{ mV})$) structures of W_i CDW are visualized under different out-of-plane field B_{\perp} at 0.3 K, showing minimal changes. Such insensitivity of the W_i CDW to B_{\perp} is further visualized by extracting the CDW amplitude ($A_{W_i}(\mathbf{r}, 3.33 \text{ mV})$, see Methods) and spatial phase ($\Phi_{W_i}(\mathbf{r}, 3.33 \text{ mV})$, see Methods) images, which also do not evolve with B_{\perp} in a systematic manner. The topological defects in Φ_{W_i} are indicated by the white and black dots. Real space correspondence between the mirror symmetric W_1 and W_3 CDW is observed clearly from their similar amplitude (A_{W_i}) distributions.



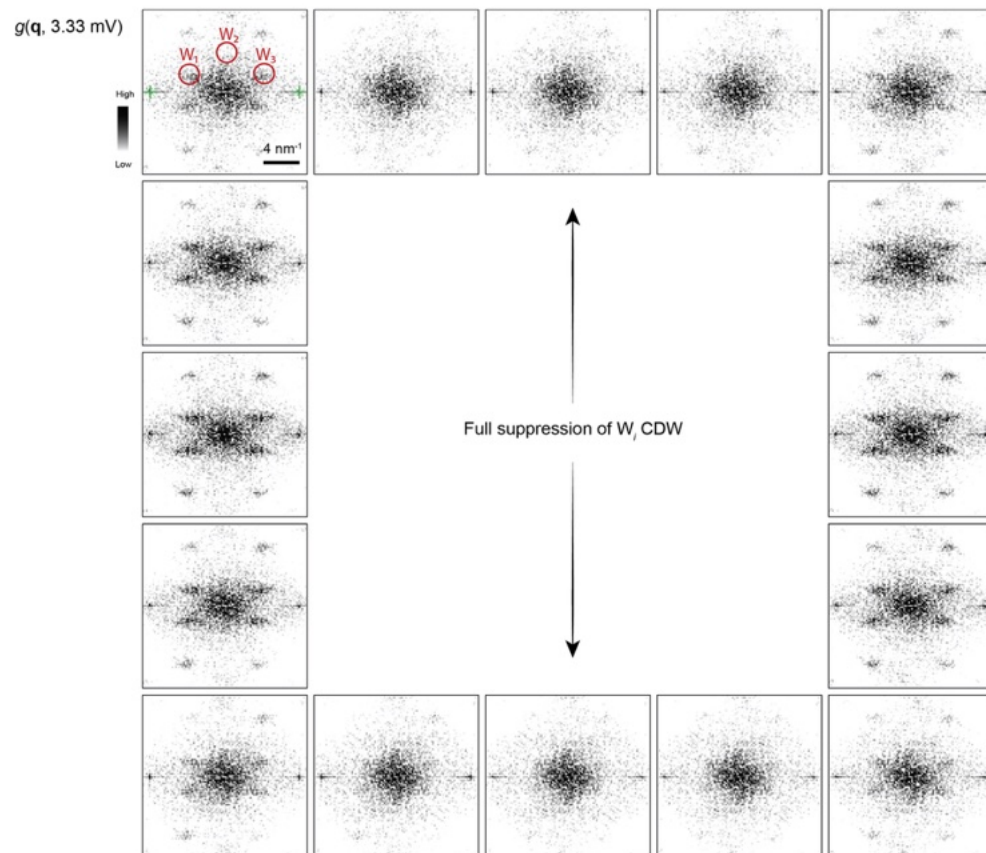
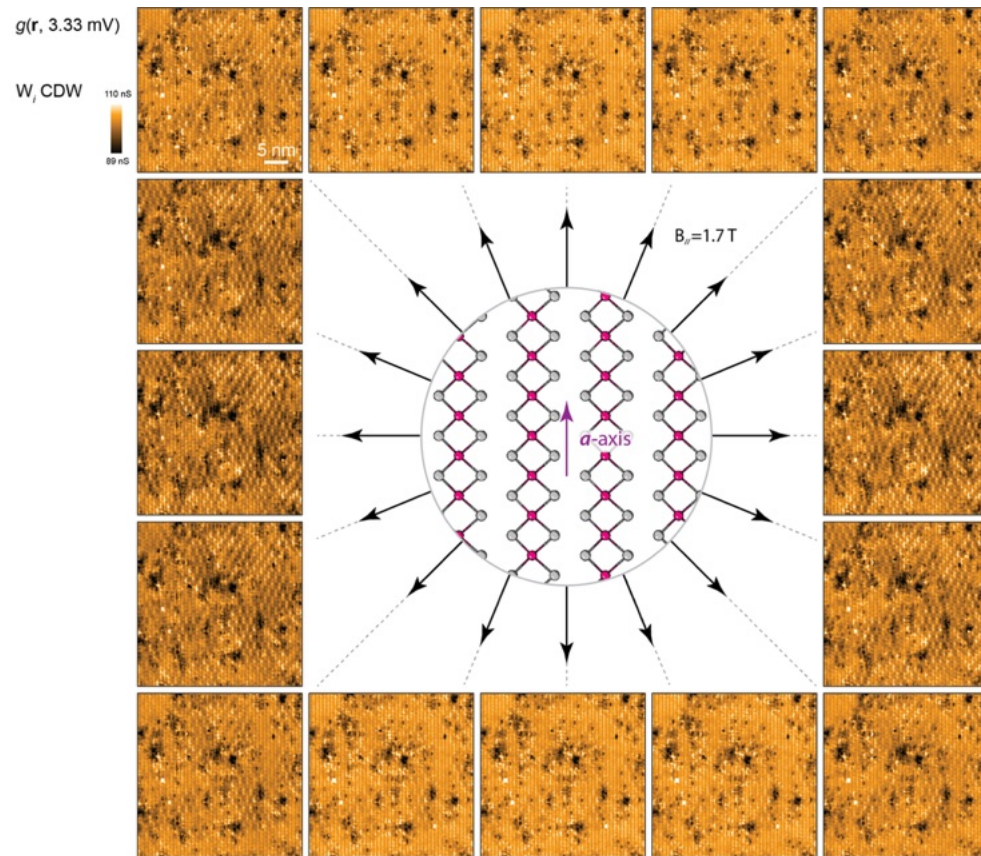
Supplementary Figure 5. Evolution of Q_i CDW as a function of B_{\perp}

In the same FOV, the momentum-space ($g(\mathbf{q}, 10 \text{ mV})$) and real-space ($g(\mathbf{r}, 10 \text{ mV})$) structures of Q_i CDW are visualized under different out-of-plane field B_{\perp} at 0.3 K, showing minimal changes. Such insensitivity of the Q_i CDW to B_{\perp} is further visualized by extracting the CDW amplitude ($A_{Q_i}(\mathbf{r}, 3.33 \text{ mV})$, see Methods) and spatial phase ($\Phi_{Q_i}(\mathbf{r}, 3.33 \text{ mV})$, see Methods) images, which also do not evolve with B_{\perp} in a systematic manner. The topological defects in Φ_{Q_i} are indicated by the white and black dots. Real space correspondence between the mirror symmetric Q_1 and Q_3 CDW is observed clearly from their similar amplitude (A_{Q_i}) distributions.



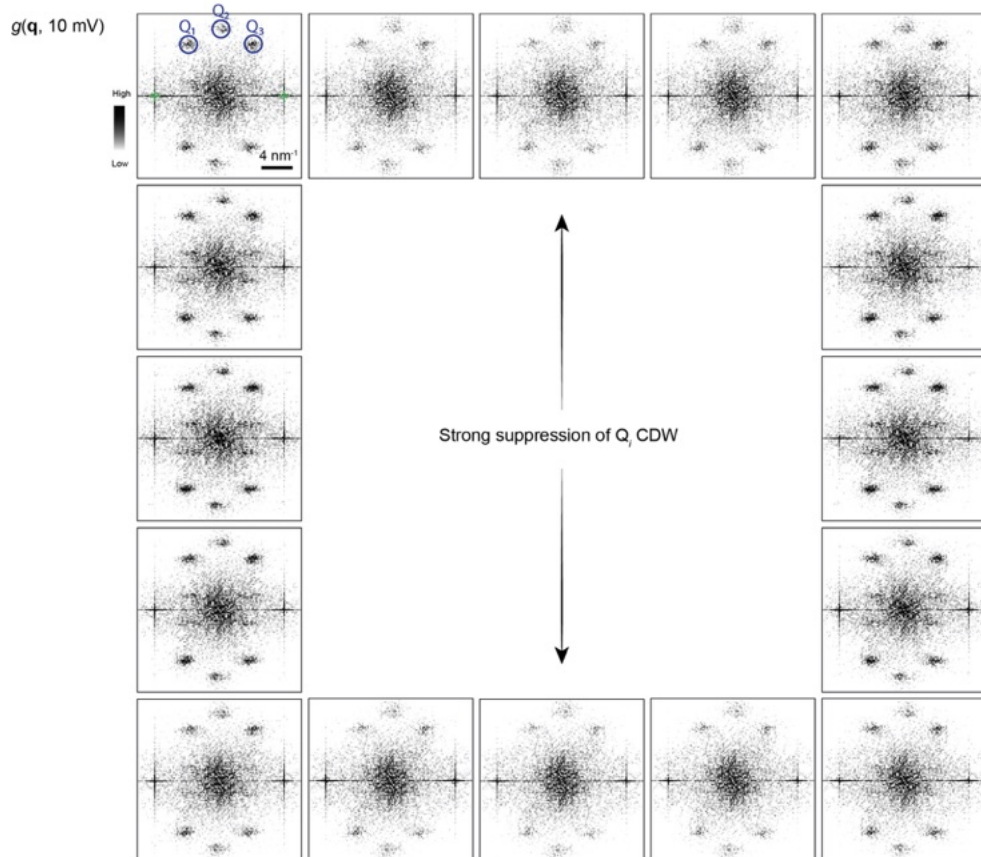
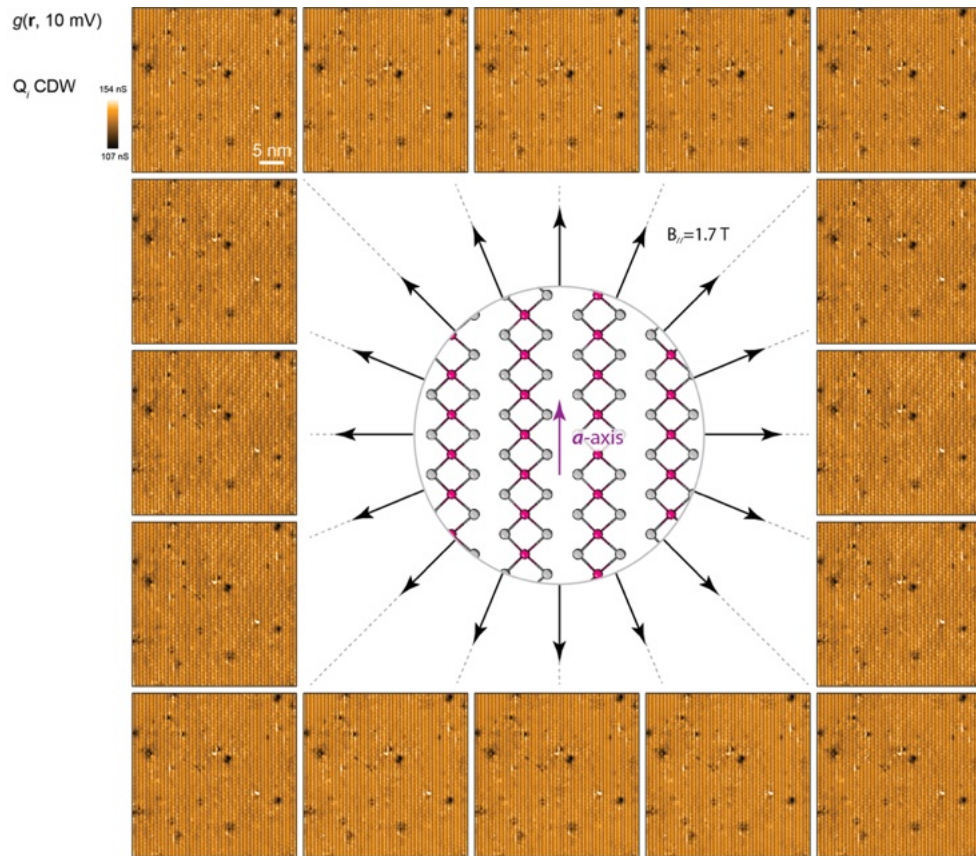
Supplementary Figure 6. Effect of CDW formfactor on the Fourier transform

a-c, Simulated triangular CDW lattices with increasing deviations from an isotropic formfactor, mimicking the staggered brick-wall pattern of W_i CDW. The FTs shown as insets clearly demonstrate the diminishing peak correspond to W_2 CDW. Therefore, the formfactor of the W_i CDW might have contributed to the much lower experimental intensity of W_2 .



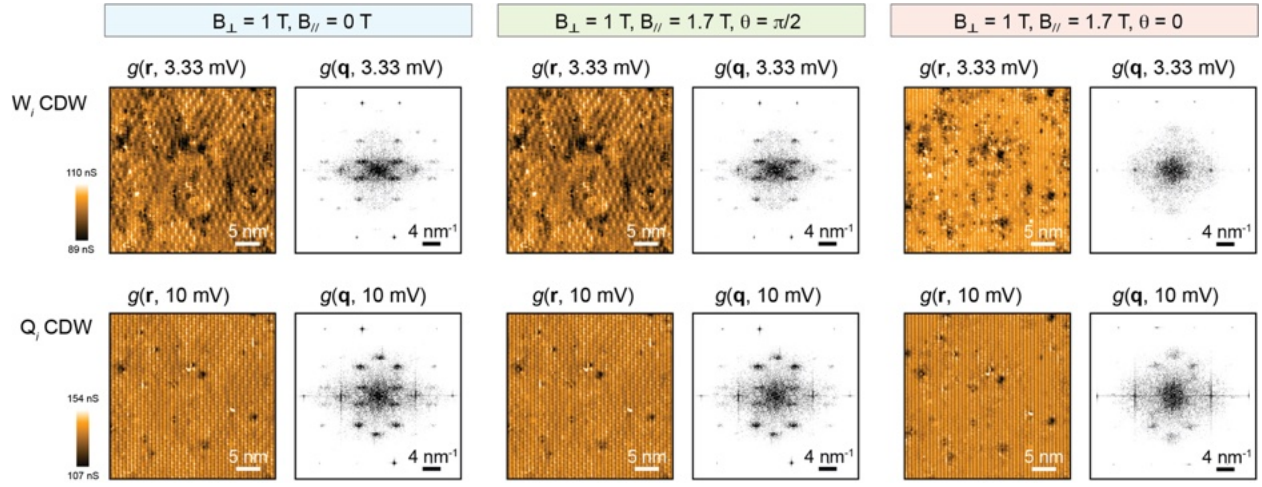
Supplementary Figure 7. In-plane field manipulation of W_i CDW

A series of $g(\mathbf{r}, 3.33 \text{ mV})$ (top) and $g(\mathbf{q}, 3.33 \text{ mV})$ (bottom) images of the same FOV but under different in-plane field (1.7 T) directions measured at 2.5 K. Complete suppression of W_i (indicated by red circles in the FTs) is observed when the field is aligned (or anti-aligned) with the a -axis of UTe_2 .



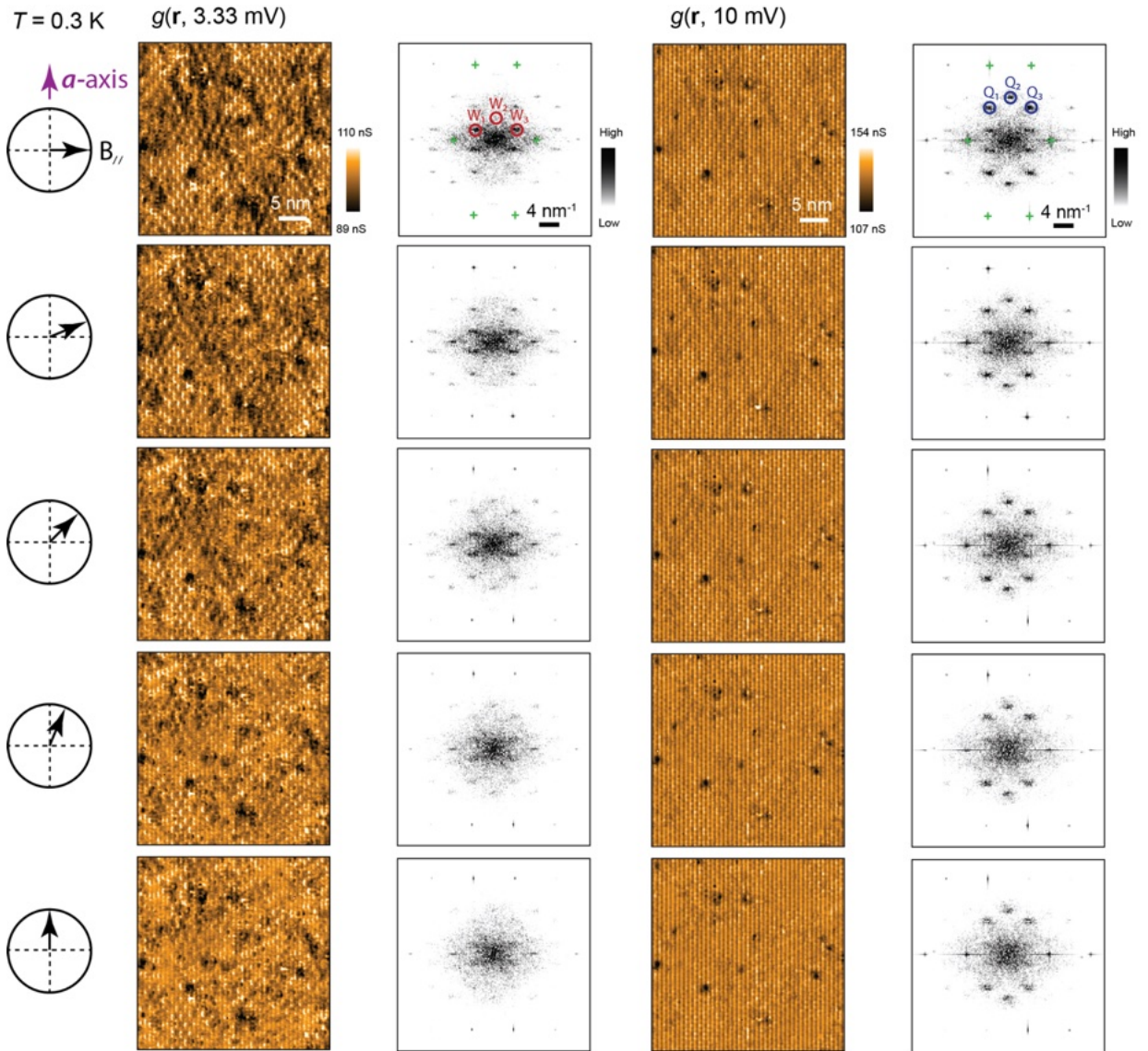
Supplementary Figure 8. In-plane field manipulation of Q_i CDW

A series of $g(\mathbf{r}, 10 \text{ mV})$ (top) and $g(\mathbf{q}, 10 \text{ mV})$ (bottom) images of the same FOV but under different in-plane field (1.7 T) directions measured at 2.5 K. Strong but not complete suppression of Q_i (indicated by blue circles in the FTs) is observed when the field is aligned (or anti-aligned) with the a -axis of UTe_2 .



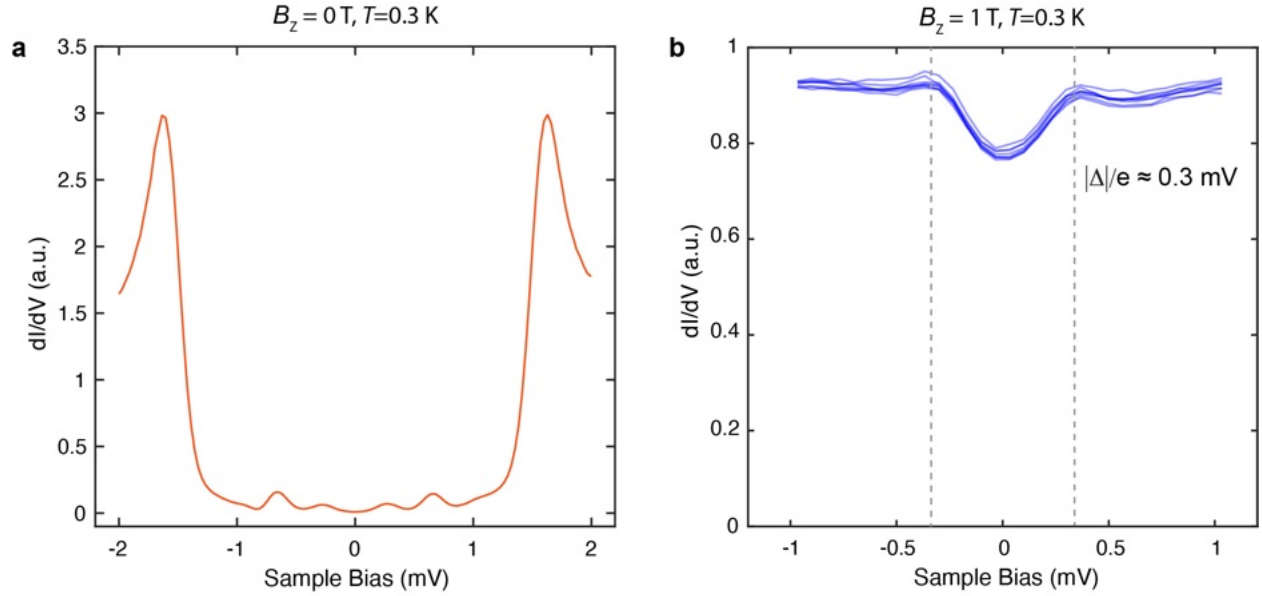
Supplementary Figure 9. Minimal influence of in-plane field along the b^* -axis

A series of $g(\mathbf{r}, 3.33 \text{ mV})$ (characterizing W_i CDW), $g(\mathbf{r}, 10 \text{ mV})$ (characterizing Q_i CDW), and their FTs are presented under different in-plane field configurations at 2.5 K: (i) $B_{\parallel} = 0$, (ii) $B_{\parallel} = 1.7 \text{ T}$ and $\theta = \pi/2$ (i.e., along the b^* -axis, Fig. 1a), and (iii) $B_{\parallel} = 1.7 \text{ T}$ and $\theta = 0$ (i.e., along the a -axis, Fig. 1a). While virtually no difference can be observed between cases (i) and (ii), demonstrating the minimal influence of in-plane field of 1.7 T along the b^* -axis, a complete (strong) suppression of the W_i and Q_i CDW takes place when B_{\parallel} is along the a -axis direction.



Supplementary Figure 10. Strong directional field sensitivity of CDWs at 0.3 K

A series of $g(\mathbf{r}, 3.33 \text{ mV})$ (characterizing W_i CDW), $g(\mathbf{r}, 10 \text{ mV})$ (characterizing Q_i CDW), and their FTs are presented under different in-plane field $B_{\parallel} = 1.5 \text{ T}$ directions with θ varying between 0 and $\pi/2$, which is indicated schematically. Similar to the observations at 2.5 K (Fig. 3, Supplementary Figs. 7,8), a complete (strong) suppression of the W_i and Q_i CDW takes place when B_{\parallel} is along the a -axis direction ($\theta = 0$).



Supplementary Figure 11. Tunneling spectroscopy between the Nb tip and UTe₂

a, Representative dI/dV spectrum of UTe₂ measured with a Nb tip at 0.3 K and zero external magnetic field ($B = 0$ T), showing the total coherence peaks and (multiple) Andreev reflection peaks as expected in a superconducting-vacuum-superconducting junction. **b**, dI/dV spectra of UTe₂ measured with a Nb tip at 0.3 K at different locations on the sample under an external field of $B_z = 1$ T (away from any vortices). Such an external field suppresses tip superconductivity and makes the tip normal but has minimal influence on UTe₂ superconductivity given its exceedingly high critical fields, thereby showing characteristic coherence peaks of high-quality UTe₂ at $\pm \frac{|\Delta|}{e} \approx 0.3$ mV. In this study, the applied field in any direction exceeds 1 T, and therefore the tip remains normal in all measurements.